RSC Advances

PAPER

View Article Online
View Journal | View Issue

Cite this: *RSC Adv.*, 2025, **15**, 37705

Green removal and waste valorization of ciprofloxacin from water using zinc–iron LDH–chia seed biocomposites: integrated adsorption, computational modeling, and electrochemical conversion

Samar M. Mahgoub,[a] Hassan A. Rudayni,[b] Ahmed A. Allam,[b] Sulaiman A. Alsalamah,[b] Asmaa Elrafey,[c] Rania Abdelazeem,[c] Amna A. Kotp,[a] Mahmoud M. Abdelsatar,[d] Rami Shafi[e] and Rehab Mahmoud *[e]

Received 14th August 2025
Accepted 12th September 2025

DOI: 10.1039/d5ra06018d

rsc.li/rsc-advances

The contamination of water with pharmaceuticals like ciprofloxacin (CFX) presents serious environmental challenges, necessitating efficient and sustainable treatment methods. This study introduces a novel green adsorbent based on zinc–iron layered double hydroxides (Zn–Fe LDH) encapsulated with chia seed mucilage for effective CFX removal. The synthesized Zn–Fe LDH/chia seed composite demonstrated exceptional efficacy, achieving 98.5% removal of CFX from water at pH 8. The adsorption process was best described by the Langmuir model, revealing a remarkably high maximum capacity of 850.05 mg g^{-1}. Thermodynamic studies confirmed the process was spontaneous and exothermic. The composite exhibited excellent regenerability, retaining 85.2% of its initial adsorption capacity after five consecutive cycles using a simple 0.1 M NaOH eluent. The composite proved to be cost-effective, with a synthesis cost of $2.033 per gram. Quantum chemical modeling revealed strong interactions ($\Delta E_{\text{int}} = -32.5$ kcal mol^{-1}) between CFX and the chia-modified LDH surface, validating the experimental results. Furthermore, the material exhibited excellent potential for waste valorization, showing current densities of 18.71 mA cm^{-2} and 15.45 mA cm^{-2} for methanol electro-oxidation before and after adsorption, respectively. A semi-pilot filtration system successfully demonstrated practical scalability, achieving >80% CFX removal from raw wastewater within 20 minutes. Greenness assessment tools (AGREEprep, BAGI, RGB12) confirmed the eco-friendly nature of the entire process, supporting circular economy goals through this low-cost, dual-function material design.

1. Introduction

Rapid population growth and expanded industrial and household activities have led to a decline in water quality, with emerging pollutants such as pharmaceuticals, dyes, pesticides, cosmetics, and persistent chemicals posing health risks by interfering with genetic expression, hormonal balance, and enzymatic processes.[1,2] The extensive use of pharmaceuticals, industrial dyes, cosmetics, pesticides, and non-biodegradable materials in daily life has led to increased water pollution. Growing concerns exist about their harmful impacts on human health and ecosystems. Pharmaceuticals and personal care products (PPCPs), widely used in human and veterinary medicine, are now recognized as emerging pollutants accumulating in aquatic environments. The widespread and poorly controlled use of antibiotics in a variety of human and animal sectors is the root cause of the increasing prevalence of pharmaceutical contaminants, particularly in aquatic ecosystems.[1] Many scientists are concerned about the widespread identification of antibiotics such as ciprofloxacin in drinking and surface waters worldwide.[3] Ciprofloxacin is a second-generation fluoroquinolone antibiotic known for its genotoxic effects. Chemically named 1-cyclopropyl-6-fluoro-4-oxo-7-piperazin-1-ylquinoline-3-carboxylic acid ($C_{17}H_{18}FN_3O_3$), it was developed in 1987 and is recognized by the World Health Organization as essential for

---

[a] Materials Science and Nanotechnology Department, Faculty of Postgraduate Studies for Advanced Sciences, Beni-Suef University, Egypt

[b] Department of Biology, College of Science, Imam Muhammad Ibn Saud Islamic University (IMSIU), Riyadh 11623, Saudi Arabia. E-mail: HARUDAYNI@imamu.edu.sa; SAAlsalamah@imamu.edu.sa

[c] Environmental Science and Industrial Development Department, Faculty of Postgraduate Studies for Advanced Sciences, Beni-Suef University, Beni-Suef, Egypt. E-mail: asmaa_elrafey@hotmail.com; raniashaban333@gmail.com

[d] Department of Geology, Faculty of Science, Beni-Suef University, Beni-Suef, Egypt. E-mail: mahmoud.abdelstar.1997@gmail.com

[e] Chemistry Department, Faculty of Science, Beni-Suef University, Beni-Suef 62511, Egypt. E-mail: rehabkhaled@science.bsu.edu.eg; abdelaty.mohamed@science.bsu.edu.eg

treating various bacterial infections. Studies report ciprofloxacin concentrations in surface waters ranging from 2.5 to 6.5 mg L^{-1}, with pharmaceutical wastewater from drug manufacturing reaching up to 31 mg L^{-1}.[2] A variety of treatment techniques, including adsorption, membrane-based separation technologies, sophisticated oxidation processes, biodegradation, ozonation, electrocoagulation, reverse osmosis, and ion exchange methods, are used to remove CFX from water.[1,4]

Adsorption is a successful process because of its main advantages, which include a high removal yield, ease of handling, fast reaction, low instrumentation and operating costs, the possibility of using a variety of adsorbents, the lack of sludge, and the absence of hazardous byproduct formation.[5] Various types of adsorbents have been studied for the removal of CFX, including carbon-based materials,[6] metal–organic frameworks, silica-based compounds, clays, polymers, biomass, agricultural waste, layered double hydroxides (LDHs), and metal oxides. Many studies have focused on removing CFX and have reported promising outcomes, as shown in Table 1. However, many of these materials face challenges related to complex synthesis, high cost, lack of environmental sustainability, or generation of spent adsorbent waste. The main challenge thus extends beyond creating efficient adsorbents to designing sustainable, low-cost, and multifunctional materials that address the entire lifecycle of the adsorption process. LDHs have gained attention due to their high adsorption capacity, low cost, and non-toxicity. Structurally, LDHs consist of positively charged bimetal hydroxide layers intercalated with water, hydroxide ions, and various anions (*e.g.*, carbonate, nitrate, organic molecules). However, LDH particles are prone to exfoliation and agglomeration, making them mechanically weak and difficult to reuse over time. Combining LDHs with more stable, larger particles like chia seeds can help overcome these limitations and improve their durability and performance.[5]

Preparing LDH materials through innovative, eco-friendly, and simple methods remains challenging. In this study, Zn–Fe LDH was chosen due to its high stability constant (~25.27) and low solubility product (62.51). The novelty of this work lies in the development of a novel biocomposite that uniquely addresses several research gaps simultaneously where it utilizes chia seed mucilage, a natural, renewable, and low-cost biopolymer, to enhance the stability and functionality of Zn–Fe LDH, aligning with green chemistry principles. Also, it moves beyond mere adsorption performance by integrating a comprehensive "waste-to-energy" valorization strategy, demonstrating the direct application of the spent adsorbent as an electrocatalyst for methanol oxidation. It validates the technology's practicality through semi-pilot scale testing with real wastewater. Finally, it provides a quantitative assessment of the method's greenness using modern tools (AGREEprep, BAGI, RGB12). This holistic approach aims not only to remove contaminants effectively but also to offer a sustainable and economically viable solution from synthesis to disposal, supporting circular economy goals. As used solid adsorbents accumulate, developing effective recycling strategies is essential worldwide to ensure sustainable material use.[6]

Table 1 Summary of previous studies that reported various adsorbents used for the removal of (CFX)

Adsorbent	Ref.	$Q_{\max}$ (mg g^{-1}) for CFX	Equilibrium time (min)	Adsorbent mass (g L^{-1})	pH	Adsorbent	Key features/Scope of the study
Zn–Fe LDH/CA	This work	850.05	240.00	0.10	8.00	Zn–Fe LDH/CA	Green biosorbent, waste valorization (electrocatalysis), semi-pilot scale validation, full greenness assessment
Fe based MOF	7	868.6	—	—	6.80	Fe based MOF	High capacity MOF.
Zeolite	8	147.06	30.00	2.50	4.50	Zeolite	
ZnO nanoparticles	9	0.16	150.00	—	4.00	ZnO nanoparticles	
Groundnut shell biosorbent	9	0.60	150.00	—	6.00	Groundnut shell biosorbent	Agricultural waste biosorbent
Chitosan/biochar hydrogel beads	7	82.05 (at 40 °C)	48.00 h	—	3.00	Chitosan/biochar hydrogel beads	Biopolymer-based adsorbent
SA/Mg_3Al LDH	10	519.60	—	—	2.00–5.00	SA/Mg_3Al LDH	Alginate/LDH composite
Magnetic Fe_3O_4/red mud-nanoparticles	11	169.49	180.00	3.00	6.00	Magnetic Fe_3O_4/red mud-nanoparticles	Magnetic separation
Ni–Al LDH	12	332.20	180.00	8.00	6.00	Ni–Al LDH	LDH-based adsorbent

Salvia hispanica, or chia seeds, is an annual herb known for its medicinal, nutritional, antioxidant, and antimicrobial properties, gaining popularity in recent years.[13]

When soaked, chia seeds develop a mucilage layer that forms a gel-like texture. This mucilage is a heteropolysaccharide composed of D-xylose, D-glucose, and glucuronic acid, providing abundant functional groups (–OH, –COOH) that are highly effective for binding pollutants *via* hydrogen bonding, electrostatic interactions, and polymer bridging. This makes it a more effective natural coagulant and adsorbent compared to other plant-based mucilages like okra or cactus, offering superior adsorption capacity and kinetics. These small, oval seeds (1–2 mm, ∼1 mg) are highly hydrophilic, absorbing up to 12 times their weight in water. Their hydrocolloids contain 5–6% mucilage, which acts as dietary fiber and provides thickening and gelling properties, helping to trap contaminants in water. Furthermore, unlike some biowastes or synthetic modifiers, chia mucilage is non-toxic, biodegradable, and requires no complex purification, contributing to a low overall synthesis cost and a minimal environmental footprint. Its performance surpasses that of other common natural polymers; for instance, it demonstrates >95% turbidity removal compared to Moringa oleifera (90–92%) and avoids the aquatic toxicity concerns associated with chitosan-based solutions.

Direct methanol fuel cells (DMFCs) are gaining attention as promising portable energy sources due to their low cost, long operational life, high energy efficiency, ease of use, and sustainability. They convert energy from commonly available fuels such as petrol, ethanol, methanol, and hydrogen, including renewable resources.[14,15] To improve methanol oxidation, various catalysts have been explored, with increasing interest in developing reliable, cost-effective, and efficient non-platinum catalysts. Carbon-based electrocatalysts stand out due to their enhanced conductivity, larger active surface area, and superior mechanical strength at a lower cost.[16] Bridging the gap between laboratory experiments and practical application, a semi-pilot scale system was constructed and evaluated. This system integrates simple, low-cost materials like sand with advanced adsorbents such as activated carbon and metal–organic frameworks (Zn–Fe LDH/CA) to effectively treat raw wastewater. This approach provides valuable insights into the feasibility, scalability, and operational performance of water filtration under real-world conditions. Building on this, the current study focuses on synthesizing a novel Zn–Fe LDH/chia seed composite *via* coprecipitation, leveraging the unique properties of chia seeds to encapsulate LDH and enhance the removal of CFX from aqueous solutions. The adsorption behavior, including equilibrium and kinetics, was extensively examined. Additionally, the structural integrity, stability, and recyclability of the composite were evaluated to ensure its suitability for sustainable water treatment applications. The environmental friendliness of the method was assessed using AGREEprep, BAGI, and RGB12 tools to highlight the greenness of the analytical process. To further support and deepen the understanding of the adsorption mechanism, this study incorporates quantum chemical modeling. Furthermore, having established the composite's adsorption efficacy, we subsequently explored its potential for circular economy application by evaluating the spent adsorbent as an electrocatalyst for methanol oxidation, thereby addressing its end-of-life cycle. This integrative approach provides insights into the experimentally observed enhancement in adsorption and offers a complete solution from pollutant removal to waste valorization.[17,18]

2. Experimental section

2.1 Materials

Hydroxyethyl cellulose (HEC, product number 434965; average molecular weight: 90 000), zinc nitrate hexahydrate ($Zn(NO_3)_2\cdot6H_2O$), and iron nitrate nonahydrate ($Fe(NO_3)_3\cdot9H_2O$) were obtained from Sigma-Aldrich. Sodium hydroxide and 37% hydrochloric acid were purchased from Scharlau (Barcelona, Spain). Both sterile and distilled water used in the experiments were of HPLC analytical grade. Ciprofloxacin (CFX, 99.92% purity) was sourced from Aarti Drugs Ltd, while chia seeds were procured from Elbana for Trade, Damanhur, El Beheira, Egypt.

2.2. Preparation of chia seed powder

Chia seeds were soaked in deionized water at a 1 : 10 ($w\ v^{-1}$) ratio and stirred at room temperature for 4 hours to allow mucilage formation. The resulting mucilage was separated by filtration and then freeze-dried using a Tofflon FDU-1100 freeze dryer (1.2 m^2 shelf capacity; Tofflon Science and Technology Co., Ltd, Shanghai, China) to obtain a dry powder.

2.3. Synthesis of Zn–Fe LDH encapsulated with ground chia seeds (Zn–Fe LDH/CA)

Zinc–iron layered double hydroxide (Zn–Fe LDH) was synthesized *via* the coprecipitation method at a constant pH. The Zn^{2+}:Fe^{3+} molar ratio was maintained at 4 : 1; this ratio was selected based on its documented high stability constant and low solubility product, which promotes the formation of a stable LDH structure.[6] Furthermore, preliminary experiments comparing ratios of 2 : 1, 3 : 1, and 4 : 1 indicated that the 4 : 1 ratio yielded the highest adsorption capacity for CFX (see SI, Table S1) and was therefore chosen for all subsequent syntheses. Briefly, one gram of powdered chia seeds was mixed with aqueous solutions of Zn^{2+} and Fe^{3+} salts and stirred for 12 hours at 25 °C to facilitate pre-adsorption and interaction. A 0.5 M NaOH solution was then gradually added using a titration system under continuous vigorous stirring until the pH reached 10.0. The mixture was aged for 24 hours at 70 °C to enhance crystallinity, then centrifuged to collect the precipitate. The solid product was washed repeatedly with distilled water and absolute ethanol until a neutral pH (∼7) of the supernatant was achieved, followed by drying in an oven at 50 °C for 24 hours.

2.4. Characterization of Zn–Fe LDH encapsulated with ground chia seeds (Zn–Fe LDH/CA)

Adsorption efficiency was evaluated using a Thermo Evolution 350 UV-Vis spectrophotometer (Thermo Fisher Scientific, Massachusetts, USA). The synthesized materials were characterized using several techniques. X-ray diffraction (XRD) was performed with a Panalytical Empyrean diffractometer equipped with Cu-Kα radiation ($\lambda = 0.154$ nm), operating at 40 kV and 35 mA, with a scanning rate of 8° min^{-1} over a 2θ range of 5°–80°. Fourier-transform infrared (FT-IR) spectroscopy was carried out using a Bruker Vertex 70 spectrometer (Germany), covering a wavenumber range of 4000–400 cm^{-1}. The particle size, dimensions, polydispersity index (PDI), and zeta potential of the Zn–Fe LDH/CA hybrid were measured using a Zetasizer Ultra (Malvern, USA).

The crystallite size (D) of the synthesized materials was calculated using the Debye–Scherrer equation as follows:

$$D = \frac{K\lambda}{\beta\cos(\theta)} \tag{1}$$

where D is the average crystallite size, K is the shape factor (typically 0.9), λ is the X-ray wavelength (0.154 nm for Cu-Kα radiation), β is the full width at half maximum (FWHM) of the diffraction peak (in radians), and θ is the Bragg angle. Bragg's law was applied to determine the interplanar spacing (d) using the following equation

$$2d\sin(\theta) = n\lambda \tag{2}$$

where n is the reflection order (typically 1 in XRD analysis), λ is the X-ray wavelength (1.5406 Å for Cu Kα radiation), and θ is the diffraction angle (half of the measured 2θ angle). To assess the impact of chia mucilage incorporation on the crystalline structure of the host matrix, the degree of crystallinity (X_c) of each synthesized sample was calculated using eqn (3):[19]

$$X_c = \frac{\text{Area of the crysralline peaks}(A_c)}{\text{Area of all peaks}(\text{crysralline}(A_c) + \text{amorphous}(A_a))} \tag{3}$$

where A_c is the area under the crystalline peaks and A_a is the area under the amorphous regions. These values were extracted through peak deconvolution using Fityk software.[20]

The microstructural features of the samples were observed using a scanning electron microscope (EVO MA10, ZEISS, Germany), and elemental distribution was evaluated *via* energy-dispersive X-ray mapping using a Quanta FEG250 SEM (FEI, USA). Nitrogen adsorption–desorption analysis was performed using a TriStar II 3020 BET analyzer (Micromeritics) to determine specific surface area, pore size distribution, and pore volume. Thermal stability was assessed *via* thermogravimetric analysis (TGA) using a Netzsch STA 409 PC/PG system under a nitrogen atmosphere at a heating rate of 10 °C min^{-1}. Finally, an Evolution 350 UV-Vis spectrophotometer (Thermo Fisher Scientific, Massachusetts, USA) was employed to quantify residual concentrations of CFX in solution.

2.5. Adsorption study

The adsorption study was conducted using a standard (CFX) stock solution of 1000 μg mL^{-1}, prepared and diluted to obtain calibration concentrations ranging from 5 to 500 μg mL^{-1}. For the adsorption experiments, 50 μg mL^{-1} of CFX solution was added to five Falcon tubes, each containing 0.05 grams of the synthesized Zn–Fe LDH/CA catalyst. The pH of each solution was adjusted to values between 3 and 10 using 0.1 N NaOH or 0.1 N HCl, and monitored with a Metrohm 751 Titrino pH meter. A parallel set of five tubes, containing only the CFX solution without the catalyst, served as controls.

All tubes were placed on an orbital shaker (SK-O330-Pro) at 250 rpm for approximately 20 hours in the dark to reach adsorption equilibrium. After incubation, the solutions were filtered using Millipore nylon syringe filters (0.22 μm pore size). The residual concentration of CFX was then measured at 270 nm using a UV-Vis spectrophotometer (UV-2600, Shimadzu). All subsequent experiments (kinetics, isotherms, thermodynamics) were performed at the identified optimal pH of 8.0.

The following equations were applied to calculate the removal efficiency and the amount of CFX adsorbed per gram of Zn–Fe LDH/CA(Q):

$$Q = (C_o - C_t) \times v/W \tag{4}$$

$$\text{Removal percentage} = (C_o - C_t) \times 100/C_o \tag{5}$$

Where C_0 represents the initial concentration of (CFX) in mg L^{-1}, C_t is the concentration of CFX at time t (mg L^{-1}), Q denotes the quantity of CFX adsorbed per gram of catalyst (mg g^{-1}), V is the volume of the CFX solution in liters (L), and W is the mass of the Zn–Fe LDH/CA catalyst in grams (g).

2.6. Waste volarization section

2.6.1. Working electrode preparation. The preparation process involved dispersing 5.0 mg of the synthesized materials before and after adsorption in 485.00 μL of isopropanol containing 15.00 μL of a 5.0 wt% Nafion solution, followed by 20 minutes of sonication. A 100 μL aliquot of the prepared suspension was then drop-cast onto graphite paper (1.5 mm thick, 1 × 1 cm^2) and allowed to dry at ambient temperature.

2.6.2. Electrochemical examination. AUTO LAB PGSTAT 302 N potentiostat/galvanostat (Metrohm, Switzerland) and NOVA 1.11 software were used to record the electrochemical measurements. The reference electrode was Ag/AgCl, the counter electrode was Pt, and the working electrode was graphite in a typical three-electrode electrochemical cell operating at room temperature. To examine the electrocatalytic effectiveness of the produced electrodes, tests were conducted in a 1 M NaOH electrolyte, both with and without methanol concentration adjustment. Within the potential range of 0–0.60 V, CV studies were conducted at scan speeds ranging from 10 to 100 mV s^{-1}. Additionally, chronoamperometry (CA) measurements were recorded for one hour at 0.6 V.

2.7. Semi-pilot filtration system

A small-scale filtration system was designed to evaluate the practical scalability of the Zn–Fe LDH/CA composite. A glass column (6 cm diameter, 40 cm height) with a total empty bed volume of 500 mL was packed with sequential layers of filtration media: a supporting gravel layer, followed by graded sand (approximately 150 g per layer, ranging from fine to coarse), a primary composite layer of activated carbon (AC) mixed with Zn–Fe LDH/CA at a weight ratio of 2 : 25 w/w (totaling 50 g), and a final top layer of coarse sand.

Raw wastewater, collected from the Tezmant wastewater treatment station (Beni Suef, Egypt), was used as the feed. A peristaltic pump (Masterflex L/S, Cole-Parmer) was used to control the inflow at two specified rates: 50 mL min^{-1} and 100 mL min^{-1}. The hydraulic retention time (HRT) for the composite layer, calculated based on the empty bed volume, was approximately 6 minutes at 50 mL min^{-1} and 3 minutes at 100 mL min^{-1}.

For the initial performance evaluation, a total volume of 3 L was processed for each flow rate condition. The drug removal efficiency was evaluated by collecting effluent samples at regular intervals and analyzing them *via* UV-Vis spectrophotometry at 270 nm for CFX. Additionally, a spike test was conducted by adding 5 μg mL^{-1} of CFX to raw wastewater. To assess the long-term adsorption capacity and saturation point, a separate experiment was conducted at a flow rate of 50 mL min^{-1}, processing over 30 L of spiked wastewater (5 μg mL^{-1} CFX). The system maintained a removal efficiency >80% for the first 20 L of treated volume, as shown in the breakthrough curve provided in SI Fig. S1.

2.8 Adsorbent regeneration and reusability study

After the adsorption experiment, the CFX-loaded Zn–Fe LDH/CA composite was recovered *via* centrifugation. Based on the adsorption mechanism and the amphoteric nature of CFX, a simple chemical regeneration method was employed.[21,22] The spent adsorbent was stirred with 50 mL of a 0.1 M sodium hydroxide (NaOH) solution for 2 hours at room temperature to desorb the CFX molecules. The regenerated adsorbent was then

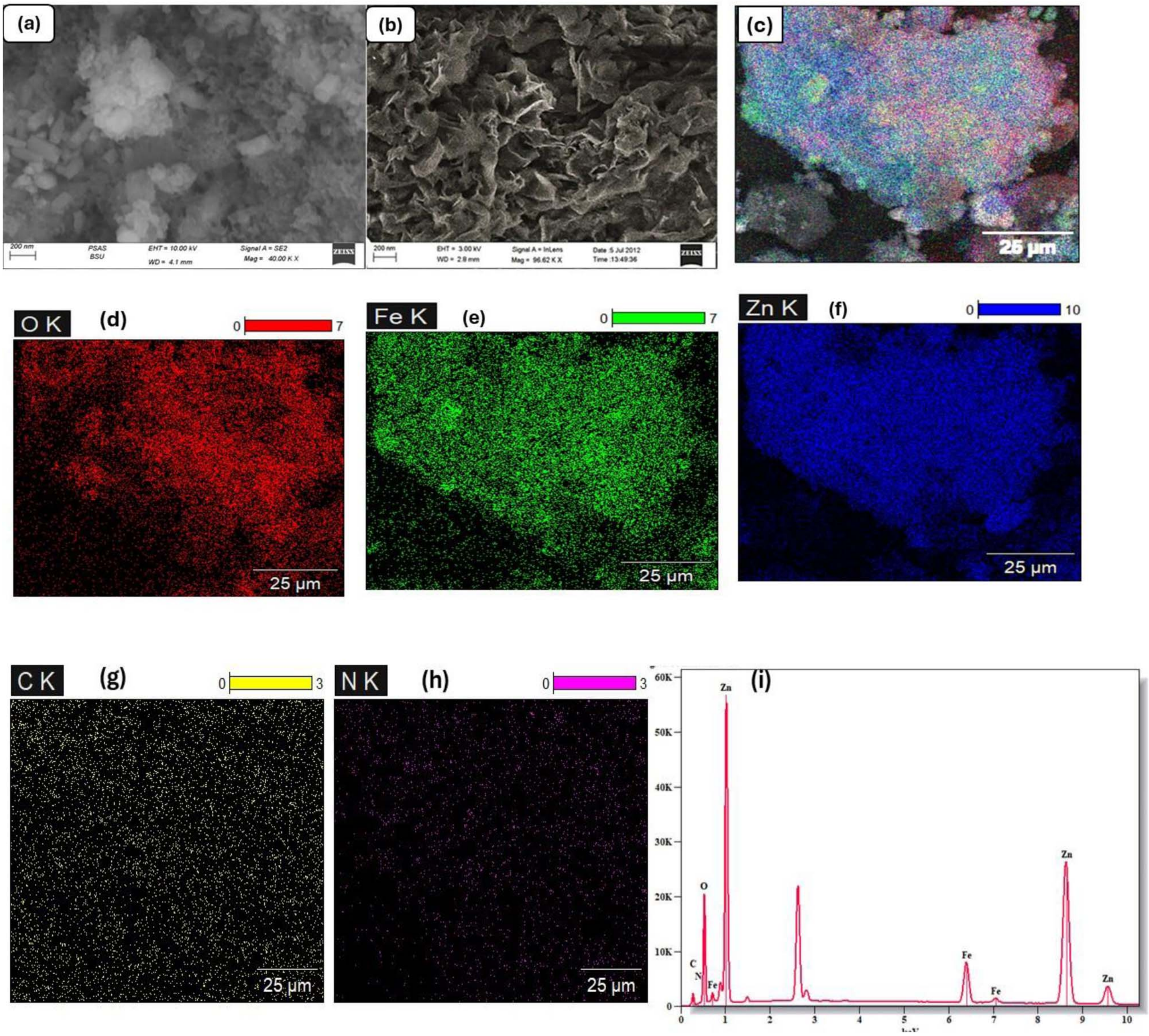

Fig. 1 FESEM images at different magnifications for (a) Zn–Fe LDH, (b) Zn–Fe LDH/CA, and 7 (c–i) EDX mapping analysis of Zn–Fe LDH/CA.

separated by centrifugation, washed thoroughly with distilled water until the supernatant reached a neutral pH, and dried overnight at 60 °C. This regeneration process was designed to be simple and low-cost.

The regenerated adsorbent was then used in subsequent adsorption cycles under the same optimal conditions (pH 8, 0.1 g/50 mL dose, 50 μg mL^{-1} initial CFX concentration). The removal efficiency was measured after each cycle to assess the reusability and stability of the Zn–Fe LDH/CA composite. The concentration of CFX in the desorption solution was also measured to calculate the desorption efficiency.

2.9. The greenness of the method

The greenness assessment tools AGREEprep, BAGI, and RGB12 were tested to evaluate how our analytical approach may impact the environment and ecosystems.

3. Results and discussion

3.1. Characterization of Zn–Fe LDH/CA

3.1.1 Morphology and surface study of Zn–Fe LDH/CA (FESEM and surface area) (energy dispersive X-ray (EDX) mapping). Upon closer inspection of the SEM image (Fig. 1(a)), the Zn–Fe LDH structure is depicted as a series of stacked plates, collectively resembling a flower-like configuration with notably high porosity. These results are in strong agreement with those previously reported by Haba A *et al.*,[14,23] reinforcing the consistency and validity of the structural characteristics identified in the SEM analysis of the Zn–Fe LDH composite. As shown in Fig. 1(b), the SEM image of the synthesized Zn–Fe LDH/CA composite displays details of the surface morphology of the LDH. The image shows a surface characterized by numerous pores and a consistently rough texture. Each LDH structure appears to be agglomerated, forming layers with a distinct plate-like morphology stacked atop one another.[24] The SEM images provide valuable insights into the morphology and microstructure of the Zn–Fe LDH/CA and Zn–Fe LDH composites, shedding light on their unique surface features and underlying structural arrangements. Additionally, EDX-map measurements were carried out for Zn–Fe LDH/CA to verify the potential impurity elements from the synthesis processes. The results of the EDX mapping microanalysis are displayed in Fig. 1(c–i). The effective synthesis of Zn–Fe LDH/CA without any further impurities was confirmed by the presence of Zn, Fe,

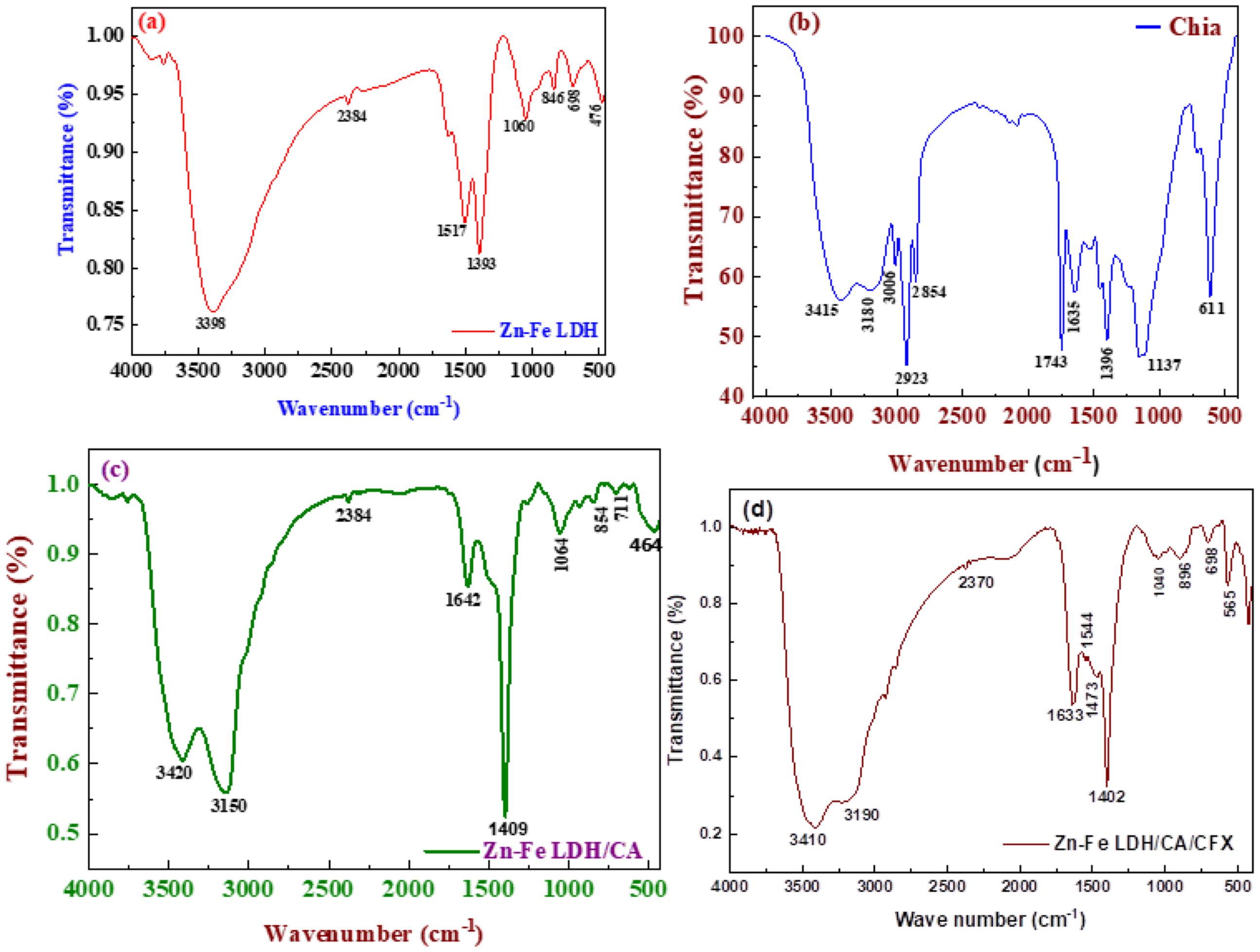

Fig. 2 FTIR results for (a) Zn–Fe LDH, (b) Chia, (c) Zn–Fe LDH/CA, and (d) Zn–Fe LDH/CA/CFX.

C, N, and O in its spectra. The elemental mapping images revealed that Zn, Fe, N, C, and O were evenly distributed throughout the material in parallel with the amounts employed in the synthesis since Zn–Fe LDH/CA was synthesized at a ratio of 4.[25]

3.1.2 Fourier transform infrared spectroscopy (FTIR).

The FTIR technique allows for verification of the chemical structure of the components before and after adsorption (Fig. 2(a–d)). Fig. 2(a) shows the FTIR transmittance spectra of the as-received Zn–Fe LDH measured at 25 °C. Next, we examine the impact of chia addition on Zn–Fe LDH and their interactions. Compared to the characteristic vibrational frequencies of the material's constituent bonds, the transmittance spectra of the samples reveal shifts in peak positions at various wavenumbers. The broad band at 3405 cm^{-1} is caused by the stretching vibration of the interlayer water molecules and the layers' hydroxyl groups.[26] The bending vibration of water (ν_{H-O-H}) is responsible for the band at 1517 cm^{-1}[24] The vibration mode of the nitrate ion (NO_3) is visible in the prominent band at 1393 cm^{-1}. Stretching modes with D3h symmetry are responsible for the bands at approximately 846 cm^{-1}, confirming the presence of NO_3 groups in the LDH interlayer. The band at 608 cm^{-1} is caused by the lattice vibration modes that correspond to the translation vibration of Zn–OH. Fig. 2(b) displays the FTIR spectra of the powdered chia seeds. The distinctive bands in the 1743–1396 cm^{-1} range for C=O bonds and the N–H and/or O–H stretching vibration of protein content are linked to the breadth of the band at 3400 cm^{-1}. The C–H stretching frequency of the methyl and methylene backbones of lipids is displayed by the bands at 2923–2854 cm^{-1}. The C=C bands can be found at 1635 cm^{-1} and 3006 cm^{-1}. The bending vibrations of methylene groups in *cis*-disubstituted olefins are the cause of the band at 611 cm^{-1}.[27] (Fig. 2(c)). The synthesis of the LDH-chia hybrid led to the elimination and displacement of certain absorption bands associated with the chia seed powder, accompanied by the appearance of a novel absorption peak at 1396.38 cm^{-1}. This newly observed band is attributed to the stretching vibrations of NO_3^- groups, which are integrated within the structural framework of the fabricated chia-LDH hybrid.[24] The typical oscillations of the metal–oxygen lattice, including M–O, M–OH, and M–O–M bonding interactions, are responsible for all vibrational bands detected below 850 cm^{-1}.[28]

3.1.3 XRD.

The Zn–Fe LDH exhibited sharp and intense diffraction peaks across the 2θ range of 6° to 80°. The basal spacing, corresponding to the combined thickness of the brucite-like layers, was measured at 0.414 nm (Fig. 3, inset), aligning well with the standard reference for nitrate LDH materials (04-018-3495). The layered structure of Zn–Fe LDH was confirmed by prominent peaks at 2θ values of 9.14°, 25.34°, 31.86°, 39.01°, 47.70°, and 56.90°. The absence of peaks indicating free hydroxide formation in the XRD pattern may be attributed to the delayed addition of sodium hydroxide during synthesis. The observed narrow peaks further indicate successful incorporation of Zn and Fe into the crystalline Zn–Fe LDH framework.[29] The plane indices were included in the XRD profile and compared with the JCPDS reference file. The XRD analysis of the LDH/CA hybrid composites, as illustrated in Fig. 3, revealed the presence of various mineralogical phases within the created materials. The synthesized Zn–Fe LDH/CA material displayed distinct diffraction peaks at (003), (006), (009), (012), (015), (018), (110), (113), (112) and (201) of Zn–Fe LDH [JCPDS No. 38-0486],[30] which were attributed to the crystallographic structure of the material (JCPDS Card No. 38-0486). The XRD pattern shows a peak for chia seed powder at approximately 2 θ = 12.37° in the two prepared samples, but another weak peak was observed only at approximately 2θ = 19.50° in the Zn–Fe LDH/CA sample. The basal plane of (003) decreased from 9.78 Å for LDH to 9.40 Å for LDH/CA.[23] This may indicate that the chia covered the surface and interacted with the surface because the *d* spacing decreased after loading.

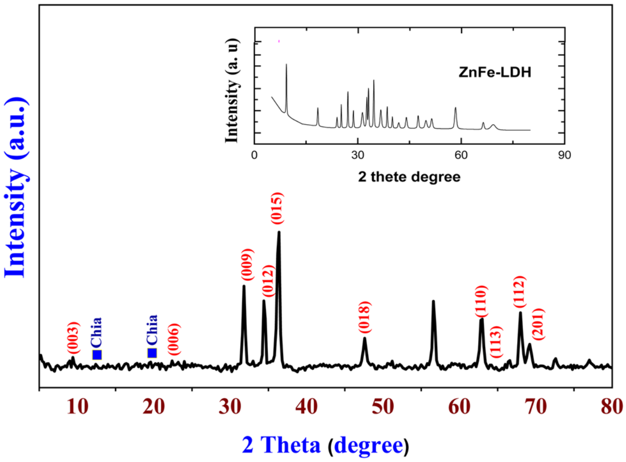

Fig. 3 XRD patterns for Zn–Fe LDH/CA and the best figure for Zn–Fe LDH.

3.1.4 BET and TGA/DTG analyses.

Assessments of nitrogen sorption have been used to determine the mesoporous nature of Zn–Fe LDH/CA. Adsorption–desorption isotherms of type IV with an H_3 hysteresis loop, a mesoporous property linked to hysteresis loops at relative pressures P/P_0 between 0.4 and 1.0, as shown in Fig. 4(a), are classified by the IUPAC with a mesopore surface of approximately 12.7 nm, a pore width of 12.666 nm, and a surface area of 41.0 $m^2\ g^{-1}$. The Zn–Fe LDH isotherm, which has a surface area of 69.23 $m^2\ g^{-1}$ and is categorized as a type IV isotherm with a type H_3 hysteresis loop, indicates that the sample is mesoporous, as illustrated in Fig. 4(b). An interaction between the material surface and electrolyte would be encouraged by the mesoporous material structure's somewhat larger surface area laterally. Additionally, the H_3 hysteresis loop implies that nonuniform slit-shaped pore formation is due to plate-like particle aggregation.[31] The observed decrease in specific surface area for the LDH/CA composite is a direct result of the encapsulation of the LDH particles within the chia seed mucilage biopolymer, which coats the surface and occupies some mesopores.[14,32] However, this physical reduction is decisively counterbalanced by the introduction of a high density of oxygen-containing functional groups (*e.g.*, –OH, –COOH) from the mucilage. These groups facilitate stronger and more specific adsorptive interactions (such as hydrogen bonding, electrostatic forces, and *n*–π

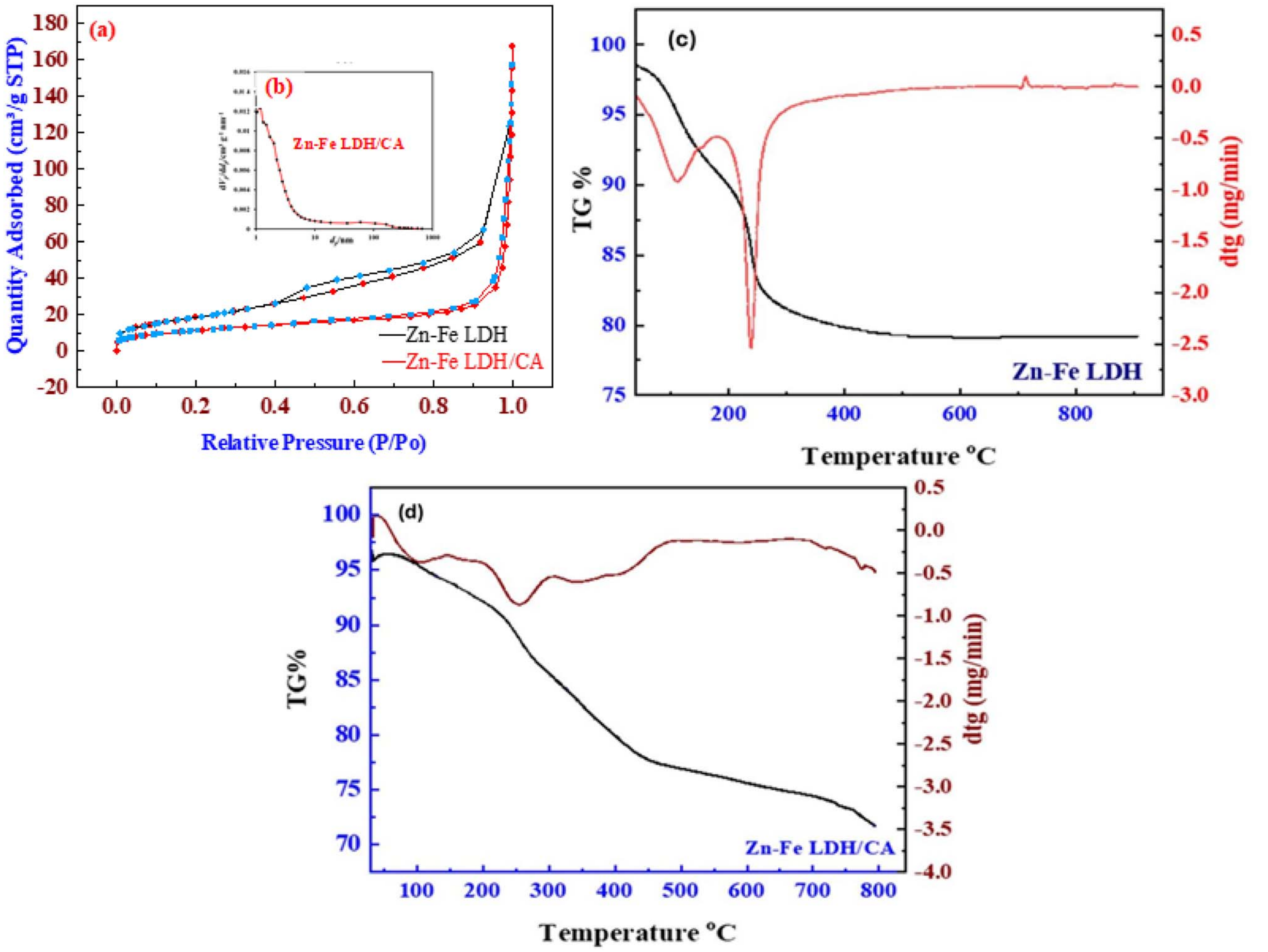

Fig. 4 (a) Adsorption–desorption isotherms of N_2; (b) pore diameter distribution curves for the various samples under study and TGA/DTG thermograms of (c) Zn–Fe LDH and (d) Zn–Fe LDH/CA.

electron donor–acceptor interactions) with the ciprofloxacin molecules.[33,34] This compensatory mechanism is confirmed by the composite's superior experimental adsorption capacity (850.05 mg g^{-1}) and the enhanced interaction energy calculated *via* quantum chemical modeling ($\Delta E_{\text{int}} = -32.5$ kcal mol^{-1} for LDH/CA *vs.* -25.0 kcal mol^{-1} for pristine LDH). Consequently, the Barrett–Joyner–Halenda (BJH) model revealed that the average pore area was 12.67 nm for the powder LDH/CA hybrid composite, which may reflect how this composite could act as a good adsorbent.

The thermal stability of the produced adsorbents was investigated by analyzing the thermal behavior of Zn–Fe LDH and Zn–Fe LDH/CA *via* TGA/DTG. Two weight loss events that are typical of LDH materials are depicted in the TGA and DTG thermograms of Zn–Fe LDH in various temperature ranges, as illustrated in Fig. 4(c and d). The initial weight loss occurs between 50 and 200 °C and is associated with the loss of physiosorbed surface water molecules. The second weight loss occurs between 250 and 550 °C and is caused by the decarboxylation of nitrate anions, which collapses the layered structure and removes interlayer anions.

The serial decomposition technique over three steps is demonstrated by the TGA and DTA results for Zn–Fe LDH/CA (Fig. 4(d)). The loss of adsorbed and interlayer water causes the first stage to occur between 40 and 150 °C. Amine groups such as NH_3 cause the second stage to occur between 150 and 300 °C, whereas the third stage occurs between 300 and 550 °C breakdown of carbonates. Changing the processing parameters, maximizing the production of valuable composites, and ensuring the stability and quality of Zn–Fe LDH/CA in a variety of applications depend on the phases of thermal breakdown.[35]

3.2 Adsorption analysis study

3.2.1 Effect of pH. The adsorption of CFX onto Zn–Fe LDH/CA is highly dependent on the pH of the solution (Fig. 5(a)). At pH 8, the charge of Zn–Fe LDH/CA was +30.24 mv, and the adsorbent surface carried a positive charge. This positive charge attracts CFX (Fig. 5(a)), which, at this pH, exists mainly in its zwitterionic form because of its two pK_a values of approximately 6.10 and 8.70. At pH 8, CFX is partially deprotonated, making it more favorable for interaction with the positively charged surface of the adsorbent.[36] This optimal pH enhances the

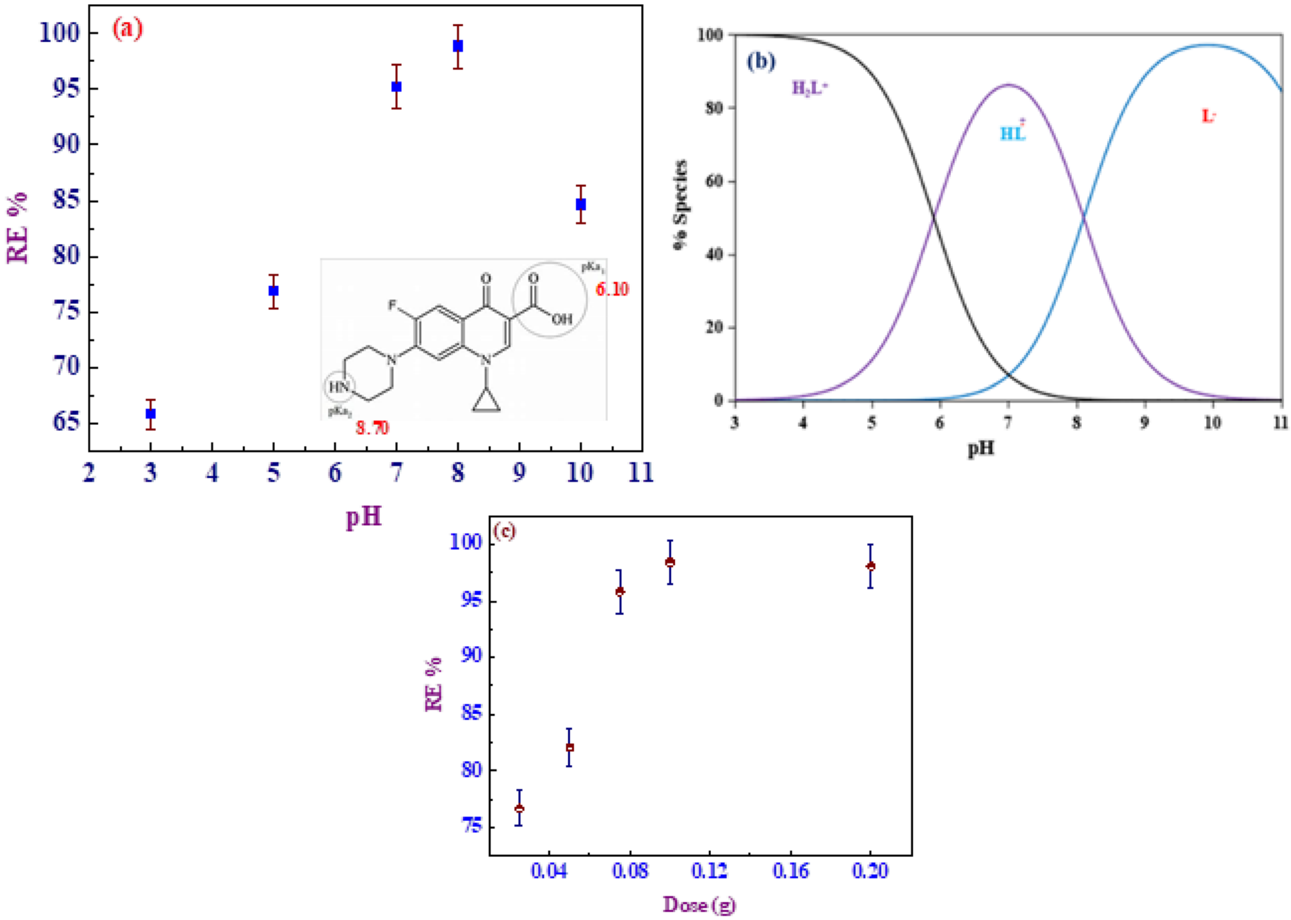

Fig. 5 (a) Adsorption of CFX at different pH values for the 50 μg mL^{-1} solution of CFX by Zn–Fe LDH/CA (0.075 g/50 mL) at 25 °C; the inset structure of CFX; (b) species distribution curve of CFX at different pH values; and (c) effect of adsorbent dose on CFX adsorption at a concentration of 50 μg mL^{-1} and a volume of 50 mL at pH 8.

electrostatic interactions that facilitate effective adsorption. In contrast, at pH 10, both the CFX and the adsorbent carry negative charges, resulting in repulsive forces that weaken adsorption. Consequently, pH 8, falling between the pK_a values of CFX, which appear from the species distribution curve (Fig. 5(b)), is ideal for maximizing adsorption (Fig. 5(a)). Additionally, the adsorption of CFX on the applied nanoadsorbent was not enhanced by the alkaline environment because negatively charged CFX molecules are competed with OH$^-$ groups. Although the adsorbent demonstrated stability within the tested range for the duration of the experiment, it is important to note that prolonged exposure to highly acidic conditions (pH < 4) is not recommended for LDH-based materials due to potential structural dissolution over time.[37,38] The low pH range (down to pH 3) was investigated primarily for mechanistic understanding of adsorption behavior under varying electrostatic conditions. For practical applications, operation near neutral to slightly basic pH conditions (*e.g.*, pH 8) is recommended to ensure long-term adsorbent stability and optimal performance.

3.2.2 Effect of dose of adsorbent. The effect of adsorbent dosage on CFX removal was investigated at pH 8.0. As shown in Fig. 5(c), the Zn–Fe LDH/CA dose was varied from 0.025 g to 0.20 g per 50 mL of solution to examine the impact of the adsorbent dose on the effectiveness of (CFX) removal. Up to 0.1 g per 50 mL, the adsorption rate dramatically increased with increasing adsorbent dose. This occurred because additional active sites for CFX adsorption are provided by a greater dose of Zn–Fe LDH/CA, increasing the overall adsorption percentage. The increase in adsorption, however, becomes negligible and stabilizes at 0.10 g per 50 mL. The saturation of the adsorbent's accessible adsorption sites is the cause of this pattern. A higher density of active sites may result from the extra adsorbent particles as the dose increases, but once these sites are fully utilized, additional adsorbent dose increases have no discernible effect on the amount of CFX eliminated. Furthermore, the particles do not clump together or become less evenly distributed in the solution at greater dosages, which may not lower the adsorbent–pollutant interaction efficiency. With a small hydrodynamic size (106.44 (±3.46) nm), a greater dose of Zn–Fe LDH/CA first increases adsorption by increasing the number of active sites and providing excellent stability in the solution.

3.2.3 Effect of temperature. This study examined the effects of temperature on adsorption efficiency at pH 8.0 by

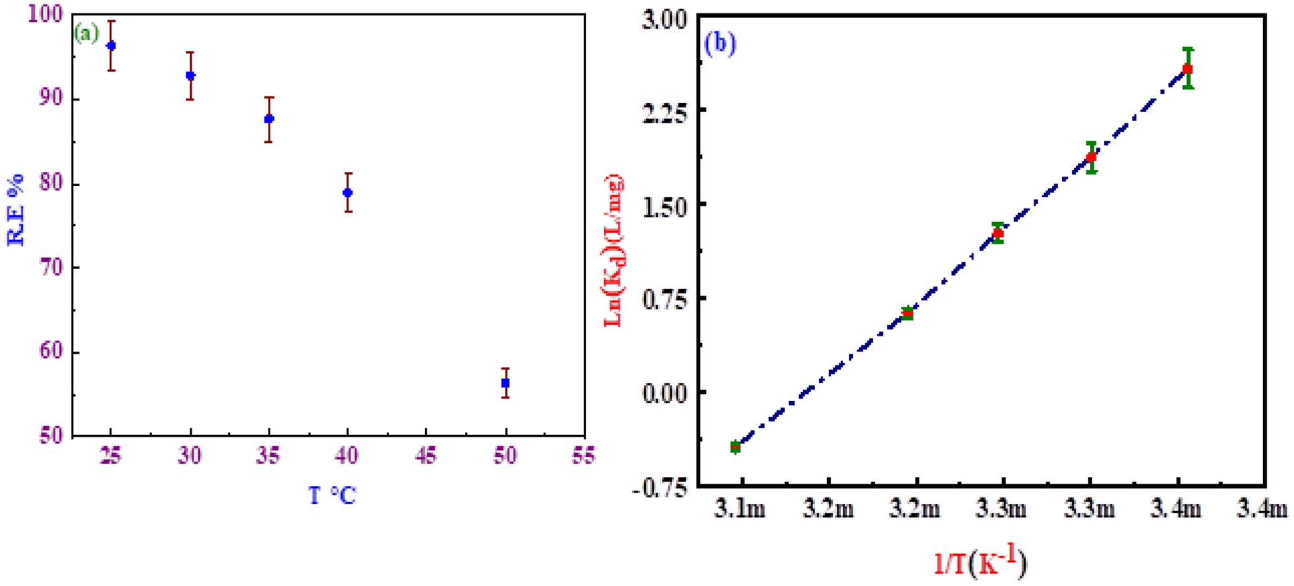

Fig. 6 (a) Effect of temperature on CFX removal efficiency at pH 8 using the LDH/CA nanocomposite and (b) for the thermodynamic parameters can be estimated by examining Ln K_d changes with temperature (K).

examining the adsorption process at a range of temperatures: 25, 30, 35, 40, and 50 °C. The removal efficiency and temperature have an inverse relationship, as shown in Fig. 6(a), which is consistent with the behavior predicted for an exothermic physical adsorption process. The system adapts to offset temperature variations according to Le Chatelier's principle, which is supported by this relationship. It appears that the adsorption is exothermic, which means that it produces heat and becomes less advantageous at higher temperatures, on the basis of the observed reduction in efficiency with increasing temperature. The weak binding interactions between CFX and the adsorbent may be the cause of the temperature-dependent decrease in adsorption efficiency. To measure these thermodynamic parameters, the results of initial experiments that computed the Gibbs free energy change ($\Delta G°$), enthalpy ($\Delta H°$), and entropy ($\Delta S°$) at various temperatures are shown in Fig. 6(b) and Table 2. The Van't Hoff equation was used to carry out these computations:[39]

$$\ln K_d = \Delta S^\circ/R - \Delta H^\circ/RT \tag{6}$$

In the van't Hoff equation, the equilibrium constant K_d is expressed in units of L mg^{-1} and represents the ratio of the adsorbate concentration in the adsorbent to its concentration in the solution at equilibrium. R is the gas constant at 8.314 J mol^{-1} K^{-1}. The term $\Delta H°$ refers to the change in adsorption enthalpy (in kJ mol^{-1}), which is a measure of the heat absorbed or released during the adsorption process. The change in entropy, or $\Delta S°$, is determined by taking the slope of the plot of ln K_d *vs.* $1/T$, where T is the temperature in Kelvin. This entropy change reveals the disorder or unpredictability associated with adsorption. The Gibbs free energy change ($\Delta G°$), which helps determine the spontaneity of the adsorption process, can be calculated *via* the following formulas. Taken together, these characteristics provide a thorough understanding of the thermodynamic components of the adsorption process:

$$\Delta G^\circ = -RT \ln K_d = \Delta H^\circ - T\Delta S^\circ \tag{7}$$

Table 2 The thermodynamic parameters of the adsorption process of CFX on LDH/CA

Material	T (K)	ΔG° (kJ mol^{-1})	ΔH° (kJ mol^{-1})	ΔS° (J mol^{-1}. K)
LDH/CA	298	−6387.80	−96.71	−302.56
	303	−4717.78		
	308	−3242.21		
	313	−1636.46		
	323	1175.26		

The plot of ln K_d *vs.* $1/T$ (K^{-1}) shows a linear relationship, as shown in Fig. 6(b). Eqn (6) was utilized to determine the change in entropy ($\Delta S°$) and the change in enthalpy ($\Delta H°$) on the basis of the slope and intercept of this figure. Eqn (7) was also used to calculate the Gibbs free energy change ($\Delta G°$). The fact that the values of $\Delta G°$, $\Delta H°$, and $\Delta S°$ are all negative suggests that the adsorption of CFX onto LDH/CA is an exothermic, spontaneous event.[39,40] This suggests that the process not only releases heat but also occurs naturally under the studied conditions.

3.2.4 Adsorption isotherms.

Adsorption isotherm experiments were conducted at pH 8.0. Adsorption isotherm models provide essential information on the maximum sorption capacity and the interactions between adsorbates and adsorbents, making them crucial for designing effective sorption systems. This study employed zinc–iron layered double hydroxide functionalized with chia seed mucilage (LDH/CA) as the adsorbent and evaluated nine nonlinear equilibrium isotherm models to analyze the experimental data. These

Table 3 Nonlinear adsorption isotherm models using LDH/CA as the adsorbent

Isotherm models	Expression	Adjustable model parameters*	Values	R^2
Two-parameters isotherm				
Langmuir	$q_e = q_{\max} \frac{K\mathrm{L}C_e}{1 + K\mathrm{L}C_e}$	$q_{\max}$	850.05	0.99
		K_{L}	0.003	
Freundlich	$q_e = K_{\mathrm{f}}\, C_e^{1/} n_{\mathrm{f}}$	K_{f}	10.83	0.99
		$1/n_{\mathrm{f}}$	0.64	
Dubinin–Radushkevich (D-R)	$q_e = (q_m) \exp(-K_{\mathrm{DR}}\varepsilon^2)$	q_m	649.03	0.97
		K_{ad}	0.02	
Three-parameters isotherm				
Langmuir-Freundlich	$q_e = \frac{q_{\max}(K_{\mathrm{LF}}C_e)^{\beta_{\mathrm{LF}}}}{1 + (K_{\mathrm{LF}}C_e)^{\beta_{\mathrm{LF}}}}$	$q_{\max}$	848.10	0.99
		K_{LF}	0.003	
		β_{LF}	1.046	
Sips	$q_e = \frac{q_{\max}(K_{\mathrm{s}}C_e)^{1/n}}{1 + (K_{\mathrm{s}}C_e)^{1/n}}$	$q_{\max}$	848.24	0.99
		K_{S}	0.0028	
		n	1.05	
Redlich–Peterson	$q_e = \frac{K_{\mathrm{RP}}C_e}{1 + a_{\mathrm{RP}}C_e^{\beta_{\mathrm{RP}}}}$		2.67	0.99
			0.001	
Toth	$q_e = \frac{K_eC_e}{[1 + (K_TC_e)^{n_T}]^{1/n_T}}$		3.09	0.99
			0.001	
			1.15	
Four-parameters isotherm				
Baudu	$q_e = \frac{q_m b_{\mathrm{o}} C_e^{1+x+y}}{[1 + b_{\mathrm{o}} C_e^{1+x}]}$	$Q_{\max}$	847.97	0.99
		b_{o}	0.0028	
		X	0.0001	
		Y	0.046	
Five-parameters isotherm				
Fritz-Schlunder	$q_e = \frac{q_{m\mathrm{FSS}} k_1 C_e^{m_1}}{[1 + k_2 C_e^{m_2}]}$	q_{mFSS}	26.19	0.99
		K_1	0.41	
		K_2	0	
		m_1	0.64	
		m_2	0	

included three two-parameter models which are Langmuir,[41] Freundlich,[42] and Dubinin–Radushkevich (D–R); four three-parameter models including: Langmuir-Freundlich, Sips, Redlich-Peterson,[43] and Toth; one four-parameter model was Baudu; and one five-parameter model was Fritz-Schlunder. Although the correlation coefficients (R^2) for several models were high and nearly identical (Table 3), the choice of the most appropriate model requires deeper statistical and mechanistic analysis beyond R^2. Among these, the Langmuir and Langmuir-Freundlich models provided the best fit, each achieving an R^2 value of 0.999 and indicating the highest adsorption capacity ($q_{\max}$) of 850.05 mg g^{-1}, as shown in Table 3 and Fig. 7(a and b). This model's superiority, confirmed by the lowest error values across multiple statistical metrics (Table 4), indicates that the adsorption process is best described as monolayer adsorption (a Langmuir characteristic) onto a surface with heterogeneous energy distribution (a Freundlich characteristic). This hybrid behavior is a direct consequence of the composite's structure, which combines the defined layered lattice of Zn–Fe LDH with the diverse functional groups (–OH, –COOH) of the chia seed mucilage.

The superior adsorption capacity of the synthesized materials is likely due to their pore structure and surface area, combined with their low-cost and environmentally sustainable synthesis, making them promising candidates for large-scale removal of (CFX) from contaminated water. Statistical analysis further revealed that the Redlich–Peterson isotherm model best described the adsorption behavior across the entire concentration range, supported by high coefficients of determination (R^2 close to unity) and low error values. Additionally, the chi-square test (χ^2) and HYBRID model results demonstrated strong agreement with experimental data over eight removal trials. It is worth noting that other statistical criteria may be influenced by factors such as the number of data points, model parameters, and the applied pressure range. All validity statistics for classical isotherm assumptions are summarized and thoroughly verified in Table 4.

3.2.5 Adsorption kinetics.

A comprehensive understanding of adsorption equilibrium is essential to elucidate how adsorbate molecules adhere to a solid surface at equilibrium, involving both the physical and chemical properties of the adsorbent and the mass transfer kinetics. This understanding is crucial for optimizing adsorbent design by clarifying the mechanism and rate of pollutant removal. In this study, five kinetic models were applied to fit the experimental data of (CFX) adsorption on LDH/CA, as summarized in Table 5 and

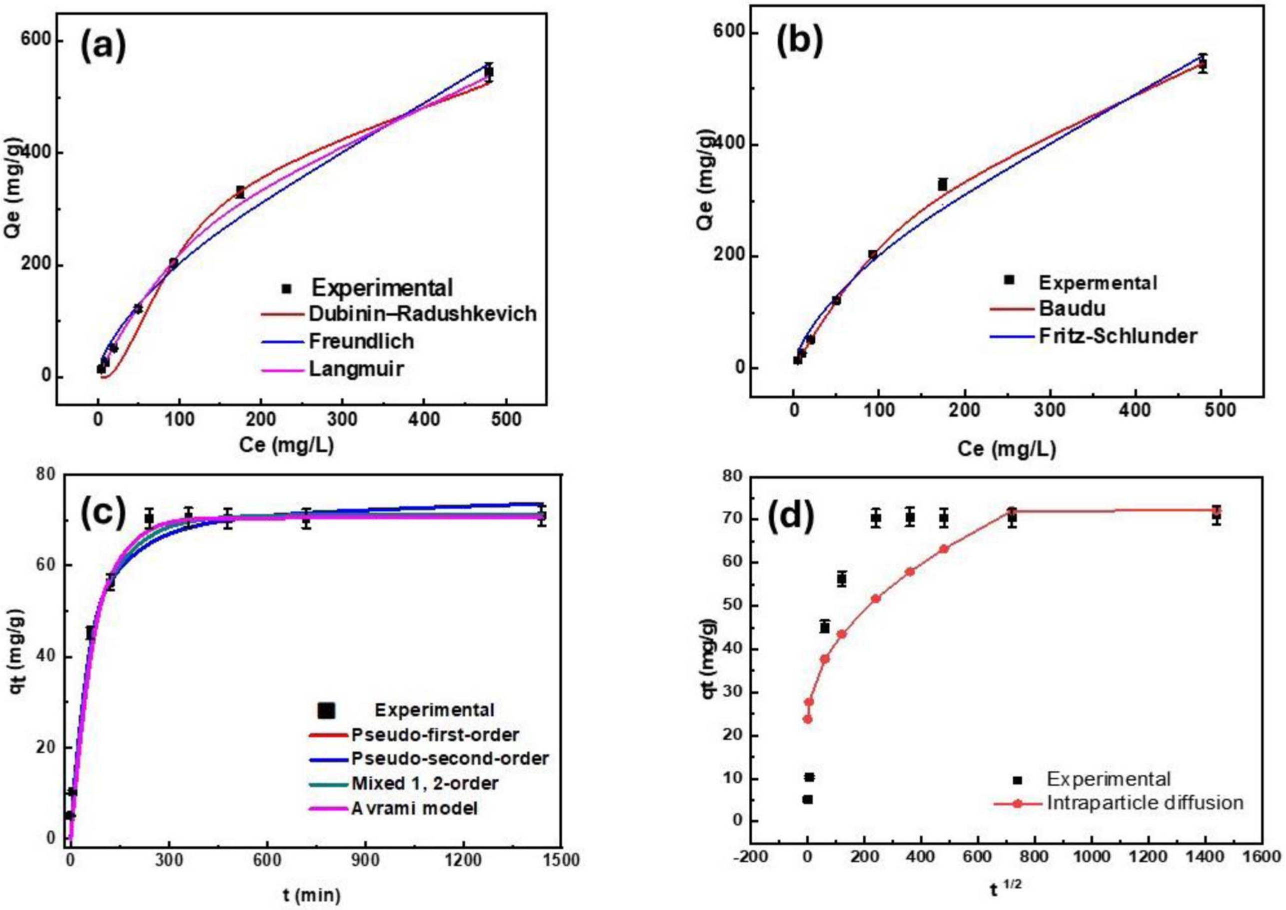

Fig. 7 (a and b) Nonlinearized fitting of different isotherm models at pH 8 for the adsorption of LDH/CA as adsorbents for CFX. (c and d) Kinetic study plots with different nonlinear kinetic models for the adsorption of LDH/CA as adsorbents for CFX.

Table 4 Presents a comprehensive overview of the error corrections identified for the CFX nonlinear classical equations that incorporate Zn–Fe LDH/CA

Function	Lang	Fran	Temkin	Dubinin	Lan. -Fran	Sips	Redlich	Toth
SSE/ERRSQ	206.67	2753.93	6263.32	35.04	16.11	35.04	11.21	35.04
χ^2	1.24	43.51	102.49	0.57	0.33	0.56	0.25	0.57
R^2	1.00	0.99	0.98	1.00	1.00	1.00	1.00	1.00
Adjusted R^2	1.00	0.97	0.93	1.00	1.00	1.00	1.00	1.00
MAE	4.55	17.75	27.57	1.87	1.29	1.86	1.07	1.86
MAPE/ARE	3.70	34.33	48.84	3.74	2.90	3.73	2.49	3.74
RMSE	5.43	19.83	29.91	2.24	1.52	2.24	1.27	2.24
RMSE_2	6.43	23.47	35.39	2.96	2.01	2.96	1.67	3.42
NRMSE	0.05	0.20	0.30	0.02	0.02	0.02	0.01	0.02
HYBRID	5.18	48.07	68.38	6.55	5.08	6.53	4.36	8.74
HYBRID_2	24.74	870.11	2049.90	14.19	8.20	14.12	6.13	18.95
HYBRID_3	1.24	43.51	102.49	0.57	0.33	0.56	0.25	0.57
MPSD	5.19	59.75	76.79	7.89	5.98	7.87	5.21	9.12
MPSD_2	0.01	1.79	2.95	0.02	0.01	0.02	0.01	0.02
SAE/EABS	31.83	124.23	192.98	13.06	9.06	13.05	7.47	13.05
RMS	4.39	50.50	64.90	5.97	4.52	5.95	3.94	5.97
NSD	0.04	0.50	0.65	0.06	0.05	0.06	0.04	0.06
ARE_2	0.19	25.50	42.12	0.36	0.20	0.35	0.16	0.36
ARE_3	1.66	19.09	24.53	2.25	1.71	2.25	1.49	2.26

depicted in Fig. 7(c and d). Results indicate that the adsorption efficiency rapidly increases during the initial phase (up to 240 minutes) due to the availability of active sites, with equilibrium reached at approximately 1600 minutes. Among the models tested, the pseudo-second-order model best described the adsorption kinetics, showing the highest correlation with

Table 5 Kinetic nonlinear model parameters for the adsorption process of CFX using Zn–Fe LDH/CA

Kinetic models	Equation	Parameters	Values
Pseudo-first-order	$q_t = q_e\,(1 - e^{-k_1 t})$	K_1	0.016
		Q_e	70.53
		R^2	0.99
Pseudo-second-order	$q_t = q_e^2 k_2 t\ 1 + q_e k_2 t$	K_2	0.0003
		Q_e	75.50
		R^2	0.99
Mixed 1,2 order	$q_t = q_e\,(1 - \exp(-k_t)\ 1{-}f_2\exp(-k_t)$	K	0.08
		Q_e	71.33
		F_2	0.64
		R^2	0.99
Avrami	$q_t = q_e[1 - \exp(-k_{av}t)^{nav}]$	Q_e	70.53
		K_{av}	0.26
		n_{av}	0.061
		R^2	0.99
Intraparticle diffusion	$q_t = k_{ip}\sqrt{t + C_{ip}}$	K_{ip}	1.80
		C_{ip}	23.75
		R^2	0.67

experimental data, whereas the intraparticle diffusion model provided a moderate fit. Key parameters such as adsorption capacities at time t (Q_t) and equilibrium (Q_e), rate constants for pseudo-first (k_1) and pseudo-second-order (k_2), as well as coefficients related to mixed-order kinetics, intraparticle diffusion, and the Avrami model, were analyzed to provide a detailed insight into the adsorption and diffusion processes governing the system.

3.3. Adsorption mechanisms

The adsorption of CFX onto Zn–Fe LDH encapsulated with ground chia seeds involves several mechanisms. First, ion exchange occurs as CFX, a negatively charged molecule in its ionized form, replaces anions in the LDH structure.[44] Electrostatic attraction also plays a role, with the negative charge of CFX interacting with positively charged sites on the LDH surface.[45] Hydrogen bonding between the carboxyl and hydroxyl groups of CFX and the LDH surface can enhance adsorption.[46] van der Waals forces contribute weakly but significantly to the overall interaction.[47] Additionally, ground chia seeds, which contain polysaccharides, proteins, and lipids, may influence adsorption by altering the surface area and interaction properties. Polysaccharides can increase surface area and binding sites[48] proteins can facilitate interactions through hydrogen bonding, and lipids can affect hydrophobicity and surface charge. More information about potential interactions between CFX and Zn–Fe LDH/CA can be greatly aided by the FTIR spectra obtained upon adsorption. Fig. 2(d)

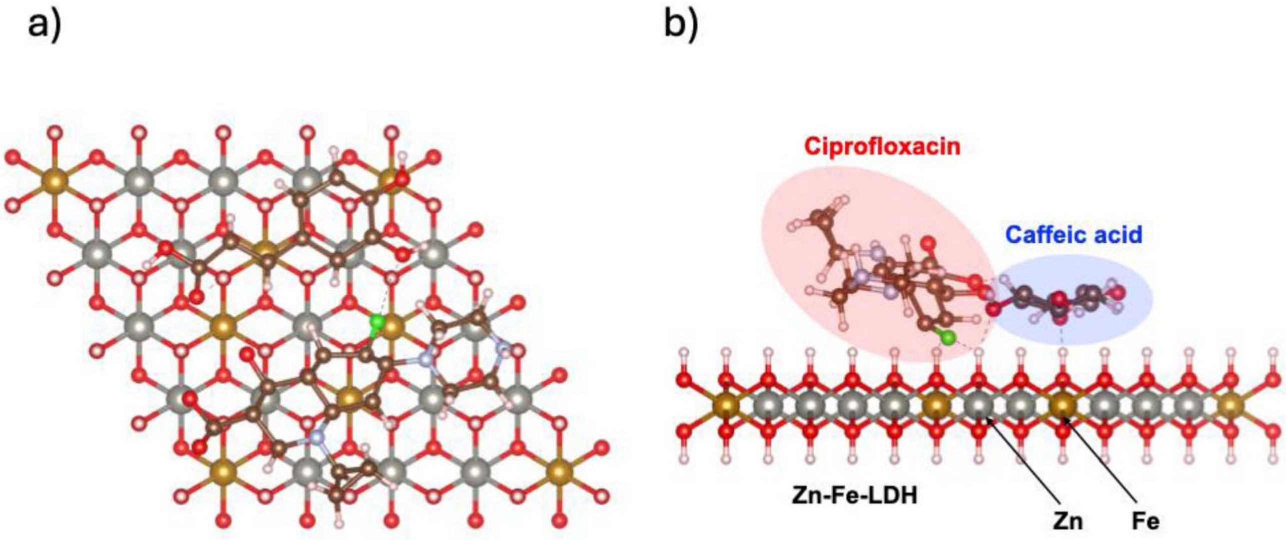

Fig. 8 (a) Top and (b) side views of DFT-optimized structure of the studied system. In the side view (panel b): the CFX ligand is highlighted by a red circle and caffeic acid by a blue circle, both located on top of the Zn–Fe LDH surface. Gray and golden spheres represent Zn^{2+} and Fe^{2+} ions, respectively, whereas green, red, brown, and pale blue spheres represent F, O, C, and N atoms, respectively. Hydrogen bonds are shown as gray dashed lines.

shows the characteristic FTIR bands following the adsorption of CFX on the composite material. With a few modifications, Zn–Fe LDH/CA/CFX displayed the same distinctive bands as Zn–Fe LDH/CA. As the 3420 cm^{-1} band shifted to 3410 cm^{-1} and became broader and 3150 cm^{-1} shifted to 3190 cm^{-1} and decreased in intensity, the 1642 cm^{-1} band shifted to 1633 cm^{-1} and increased in intensity, whereas the 1409 cm^{-1} band shifted to 1402 cm^{-1} and decreased in intensity. The vibration absorption of the CH_2 on the benzene ring is responsible for the peaks at 1633, 1544, and 1473 cm^{-1}, which are distinctive peaks for CFX and exist in the composite/CFX and do not appear in the composite alone. Additionally, the slight alterations in the O–H and N–H stretching regions ($\sim$3400 cm^{-1}) suggest that the CFX and the composite material could participate in hydrogen bonding.

To quantitatively validate the proposed mechanisms and provide a crucial link between computation and experiment, the quantum chemical interaction energy ($\Delta E_{\text{int}} = -32.5$ kcal mol^{-1}) was compared with the experimentally determined enthalpy change ($\Delta H° = -96.71$ kJ mol^{-1}, equivalent to -23.1 kcal mol^{-1}) from van't Hoff analysis (Table 2). The strong, favorable interaction energy computed for the CFX-LDH/CA system is in excellent agreement with the significant exothermic enthalpy change observed experimentally. The computed value is more negative, which is expected as the DFT calculation models a direct, gas-phase interaction between a single CFX molecule and a specific, optimized surface site, effectively representing the enthalpy change at 0 K without entropic or solvation effects. The experimental $\Delta H°$ is an average value measured in solution across all available sites and includes real-world effects. The close correlation (both large and negative) between these independent values provides robust, multi-faceted evidence that the adsorption is highly exothermic and strongly supports the proposed mechanism where chia mucilage functionalization enhances the binding strength of CFX to the LDH surface. To investigate the adsorption interactions of CFX on both pristine Zn–Fe LDH and Zn–Fe LDH functionalized with (CA), quantum chemical modeling was performed *via* the ORCA 6.0 software package.[18] The HF-3c method with Grimme's including D3BJ dispersion correction was employed for geometry optimizations to capture intermolecular interactions efficiently, followed by single-point energy

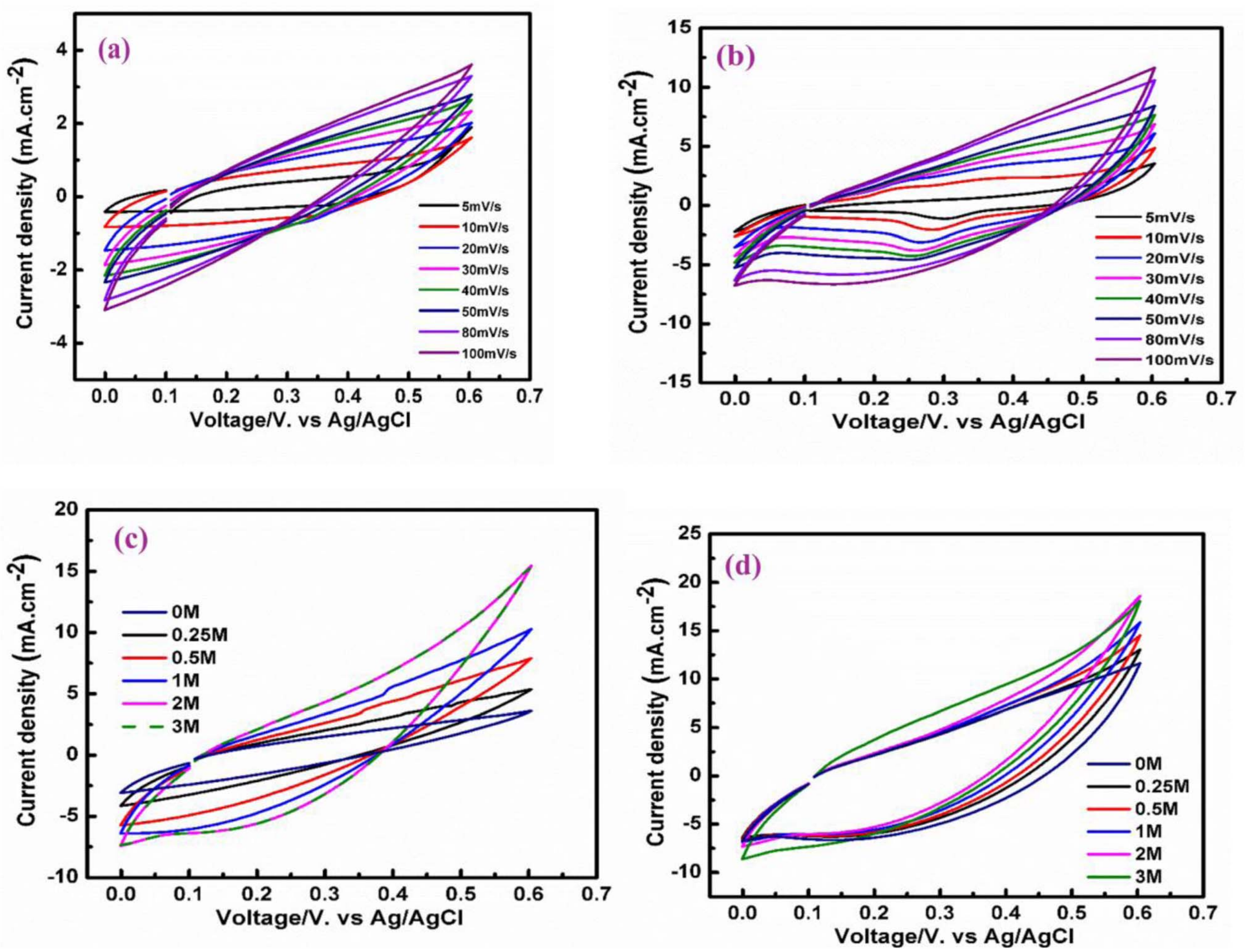

Fig. 9 Effect of scan rate on (a) CV curves of Zn–Fe LDH/CA before, (b) Zn–Fe LDH/CA after adsorption and effect of methanol concentration on (C) CV of Zn–Fe LDH/CA before and (D) Zn–Fe LDH/CA after adsorption.

calculations.[49] All calculations incorporated the conductor-like polarizable continuum model (CPCM, water) to simulate an aqueous environment relevant to adsorption processes.[50] The Zn–Fe LDH was modeled as a $[Fe_8Zn_{17}(OH)_{70}]^{12-}$ cluster (Zn: Fe $\approx 4:1$), whereas CA was represented by caffeic acid $[C_9H_8O_4]$ to mimic its hydroxyl and carboxylate groups, which facilitate hydrogen bonding and electrostatic interactions with the LDH surface and CFX. CFX $[C_{17}H_{17}O_3N_3F]^-$ was optimized in its zwitterionic form, which is dominant at neutral pH. The composite systems (Zn–Fe LDH/CA, Zn–Fe LDH/CFX, Zn–Fe LDH/CA-CFX) were constructed, and the optimized whole system Zn–Fe LDH/CA-CFX geometry is shown in Fig. 8. The interaction energies for CFX adsorption on Zn–Fe LDH functionalized with caffeic acid (representing CA) were calculated *via* the supermolecular approach with BSSE correction as follows:

$$\Delta E_{\text{int}} = E_{\text{complex}} - \sum E_{\text{fragment}}$$

The interaction energy for CFX on pristine Zn Fe-LDH is -25.0 kcal mol^{-1}, driven primarily by Zn^{2+}-OH-carboxylate, π–π stacking interactions. Functionalization with caffeic acid enhances the interaction energy to -32.5 kcal mol^{-1} for CFX on Zn–Fe LDH/CA, a modest ~30% improvement attributed to additional hydrogen bonding between CFX's piperazine group and caffeic acid's hydroxyl/carboxylate moieties, alongside strengthened electrostatic interactions. The caffeic acid-Zn-Fe LDH interaction energy of -15.0 kcal mol^{-1} reflects stable grafting of caffeic acid (and consequently CA) onto the LDH surface *via* hydrogen bonds and electrostatics. This computed enhancement directly corroborates the experimental observation of a higher adsorption capacity for the chia-modified composite. These interaction energies confirm that caffeic acid functionalization enhances CFX adsorption, making Zn–Fe LDH/caffeic acid a promising, eco-friendly adsorbent for antibiotic removal from aqueous environments.

3.4. Recycling study *via* a methanol fuel cell

3.4.1. Effects of different scan rates and different methanol concentrations on electrochemical oxidation. Cyclic voltammetry was utilized to examine the scan rate-dependent electrochemical response, applying the potential sweep technique over a potential range of 0.0 V to 0.60 V. The scan rate was incrementally adjusted between 5 and 100 mV s^{-1} in an alkaline electrolyte. As illustrated in Fig. 9(a and b). These data show that increasing the scan rate from 5 to 100 mV s^{-1} enhances the current density for both Zn–Fe LDH/CA before and after. This tendency can be attributed to more electroactive species reaching the electrode surface as the scan rate increased, which produced an increase in the current density. Fig. 12(a, c and d) shows how the methanol concentration affects the anode current density and electrocatalytic activity. These findings indicate that adjusting the methanol ratio has a pronounced effect on fuel cell efficiency. The study evaluated the cyclic voltammetry (CV) current density at a scan rate of 100 mV s^{-1} with methanol concentrations ranging from 0.25 M to 3.0 M. The experimental findings indicated a direct dependency of the peak current density on the methanol concentration during electrooxidation, albeit with observed limitations. The peak current density rose significantly as the methanol concentration increased from 0.25 M to 3.0 M, reaching an optimum at 2 M, after which no further substantial changes were observed. An inverse correlation exists between the methanol concentration and the oxidation peak current density, where higher methanol levels result in lower current densities. This phenomenon is linked to the buildup of methanol oxidation intermediates on the electrocatalyst surface, which progressively occupies active sites and induces catalyst poisoning. Owing to the restricted diffusion of reactant species, the interaction with the electrocatalyst is hindered, causing a noticeable decrease in the anodic peak current density.[51] Table 6 shows the different current density values for methanol electro-oxidation that our current work has produced.

3.4.2. Electrochemical reaction, stability, and electrochemical impedance spectroscopy measurements. The electrochemical performance of the fabricated electrodes in the methanol oxidation reaction (MOR) is demonstrated in Fig. 10(a). The electrodes exhibit peak activity at 18.71 mA cm^{-2}, but following CFX removal, the current density decreases to 15.45 mA cm^{-2}. This decrease in electrochemical efficiency may be associated with the occupation of active sites on the used adsorbents, which hinder catalytic activity and limit the availability of reaction sites. Electrode stability in the methanol oxidation reaction (MOR) is a crucial parameter influencing its potential for large-scale commercial deployment.

Chronoamperometric measurements were used to evaluate electrode stability. Fig. 10(b) shows that both electrodes have good stability against MOR, with current density retention reaching 66% and 53% before and after MOR, respectively. Using EIS measurements in (1 M) NaOH or 2 M MeOH for both samples and the pretest at 0.6 V *vs.* Ag/AgCl and in the frequency range of 0.01–100000 Hz with an AC amplitude of 10 mV and a 1 s equilibrium time, the electrode resistance was examined. An angled line in the low-frequency range and a small quasi semi-circle in the high-frequency range represent the Nyquist plots. A small quasi semi-circle affects the charge transfer resistance (R_{ct}) at the electrode/electrolyte interface. Fig. 10(d)

Table 6 Electro-oxidative activity reported in this work

Material	Methanol concentration (M)	Scan rate (mV S^{-1})	Current density (mA cm^{-2})
Zn–Fe LDH/CA	2.0	100	18.71
Zn–Fe LDH/CA/CFX	2.0	100	15.45

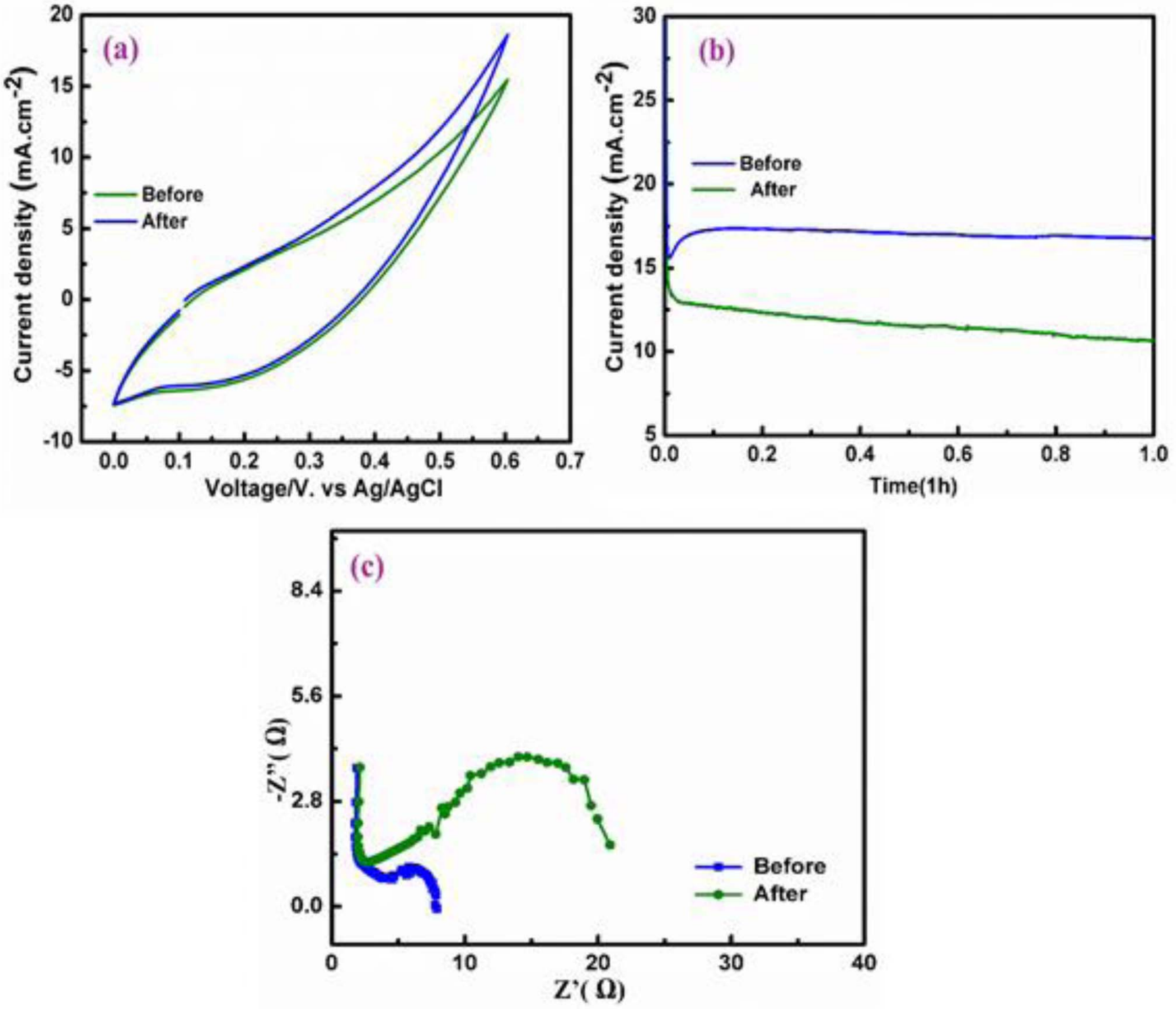

Fig. 10 (a) CV curves of the Zn–Fe LDH/CA samples before and after, (b) chronoamperometric measurements for 1 h, cycles, and (c) electrode resistance EIS measurements in 1 M NaOH and 2 M MeOH.

displays the Nyquist plots of the samples before and after sintering. The resistances to charge transfer, or R_{ct}, are 8 Ω and 20 Ω, respectively.

3.5. Cost estimation

The cost estimation of the prepared adsorbent is a crucial component of performance analysis since economical

Table 7 Cost estimation of the preparation of Zn–Fe LDH/CA

Material	Quantity purchased (g)	Total amount spent (USD)	Purchasing cost (USD per g)	Used quantity (g or mL)	Cost of used quantity (USD)
Zn (NO$_3$) $_2$6H$_2$O	25	35	1.4	7.57	10.59
Fe(NO$_3$)$_3$9H$_2$O	500	29.16	0.058	4	0.232
Sodium hydroxide	25	21.90	0.876	4	3.504
chia seeds	200	2	0.01	1	0.01
Equipment	Time (H)	Max. Power (kW)	Unit cost of power	Energy cost	
Magnetic stirring	12	1	0.24	2.88	
Dryer	12	1	0.24	2.88	
Centrifuge	1	1	0.24	0.24	
		Total yield cost = 20.33 USD for 10 g	Total yield cost = 2.033 USD per g		

adsorbents offer significant advantages for practical implementation. The detailed cost breakdown for synthesizing the Zn–Fe LDH/CA nanocomposite is presented in Table 7. Based on current market prices, the estimated unit costs of sodium hydroxide, zinc nitrate, ferric nitrate, and chia seeds are 10.59, 0.232, 3.504, and 0.01 USD/g, respectively. The required quantities for producing 10 g of final composite are 7.57, 4, 4, and 1 g of these materials, respectively.

Beyond material costs, we accounted for energy consumption during synthesis. The magnetic stirrer operated for 12 hours and the dryer for a comparable duration, with energy costs calculated based on maximum power ratings and a utility rate of 0.24 USD kWh^{-1}. The centrifugation and washing processes were also included in the energy assessment. The total production cost for 10 g of composite was calculated as 20.33 USD, resulting in a synthesis cost of 2.033 USD g^{-1}.

While absolute cost provides one metric, a more meaningful evaluation considers performance efficiency relative to cost. We therefore calculated the adsorption capacity per unit cost ($q_{\max}$/cost) as a key economic indicator. As shown in Tables 8 and 9, our Zn–Fe LDH/CA composite demonstrates an exceptional ratio of 418.1 mg g^{-1} USD^{-1}, significantly outperforming other recently reported adsorbents. This superior economic efficiency stems from the synergistic combination of high adsorption capacity (850.05 mg g^{-1} for CFX) and moderate synthesis costs, highlighting the practical advantage of our green approach using chia seed mucilage for water treatment applications.

3.6. Semi-pilot scale experiments

The semi pilot filtration system effectively removed CFX from raw wastewater through a synergistic mechanism combining physical filtration, adsorption, and chemical interactions. Graded sand served as a mechanical barrier for suspended solids and turbidity, whereas activated carbon provided an extensive surface area for the adsorption of organic pollutants and drug residues. The prepared component contributed to enhanced adsorption through its porous structure, metal-chelating capabilities, and π–π interactions with the CFX molecules. Additionally, the sponge layer helped retain fine particles, ensuring the clarity and stability of the flow. At a flow rate of 50 mL min^{-1}, the system achieved a substantial reduction in CFX absorbance from an initial value of 0.185 to 0.03, indicating efficient removal. However, increasing the flow rate to 100 mL min^{-1} led to a decreased removal efficiency (absorbance = 0.07), likely due to the reduced contact time between the contaminant and the adsorptive media.

A simulated spike test conducted with 5 μg mL^{-1} CFX in raw wastewater revealed a decrease in absorbance from 0.381 (blank sample) to 0.085, further validating the system's performance under relatively high contaminant loads. In a time-course experiment (samples collected every 5 minutes for 30 minutes), the CFX concentrations decreased steadily from 1.367 to 0.143, with over 80% removal achieved within the first 20 minutes. These results suggest that the system achieves >80% removal in the early stages of treatment, stabilizing after ~20 min, possibly due to saturation of adsorption sites or equilibrium.

These findings align with the literature on hybrid materials, which have shown high efficiency in removing pharmaceuticals from water matrices because of their combined adsorption and chemical interaction capabilities.[55]

3.7 Regeneration and reusability of the adsorbent

The economic feasibility and environmental sustainability of an adsorbent are critically dependent on its ability to be regenerated and reused multiple times without a significant loss in performance. A simple and effective regeneration method is therefore essential.[21,56]

Table 8 Economic comparison of adsorption performance between Zn–Fe LDH/CA and other reported adsorbents

Material	Synthesis cost (USD per g)	$q_{\max}$ (mg g^{-1})	Performance-to-cost ratio (mg per g per USD)	Reference
Zn Al LDH/PU/O-Pom	0.90	350.0[a]	388.9	52
Cellulose-based Co–Fe LDH	2.55	140.2[a]	55.0	53
ZnFe-LDH	8.14	200.0[a]	24.6	23
Zn–Fe LDH	3.12	185.0[a]	59.3	54
Zn–Fe LDH/PANI	12.48	213.0[a]	17.1	54
Co/Ni/Cu–NH_2BDC MOF	7.00	225.0[a]	32.1	52
Zn–Fe LDH/CA	2.033	850.05	418.1	This work

[a] $q_{\max}$ values marked with represent adsorption capacities for representative pollutants (antibiotics or dyes) as reported in respective studies. The performance-to-cost ratio provides a standardized comparison of economic efficiency across different adsorbent systems.

Table 9 Removal efficiency of CFX under various conditions using the semi pilot scale system

Condition	Initial absorbance	Final absorbance	% Removal
50 mL min^{-1} flow rate	0.185	0.030	83.8%
100 mL min^{-1} flow rate	0.185	0.070	62.2%
5 μg mL^{-1} spike test (blank)	0.381	0.085	77.7%
Time-based (30 min)	1.367 → 0.143	—	~89.5%

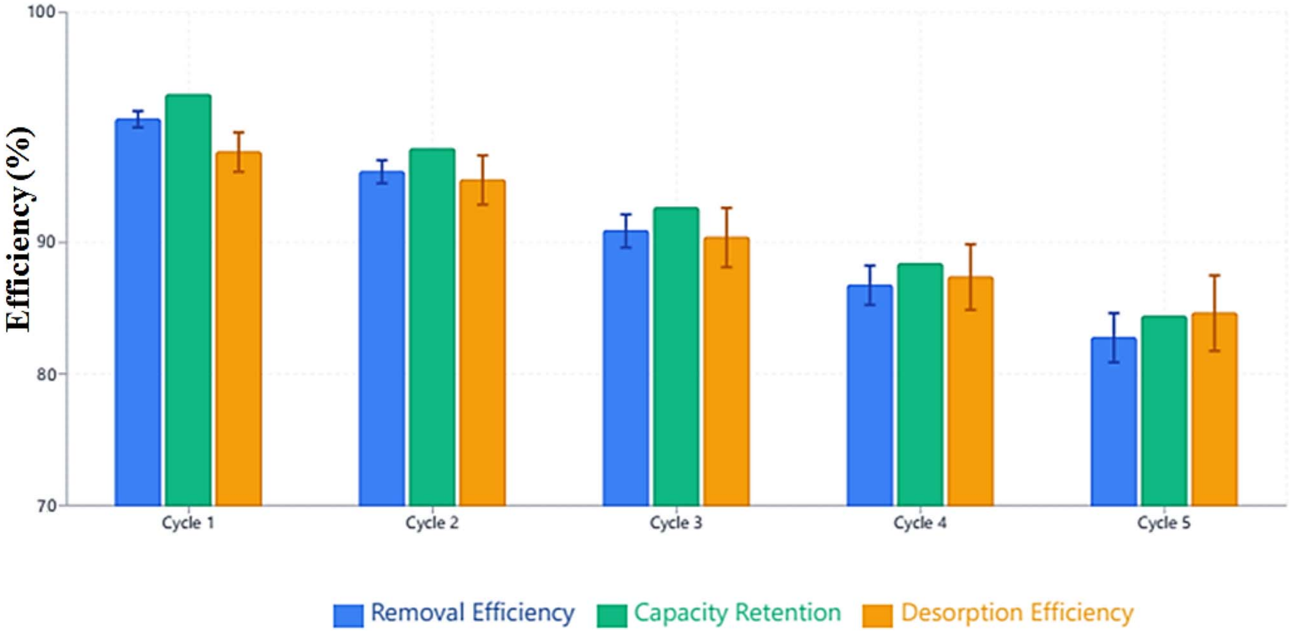

Fig. 11 Reusability of Zn–Fe LDH/CA composite for CFX removal over five consecutive adsorption–desorption cycles.

Given that the adsorption was optimal at pH 8 where electrostatic interactions play a key role, a mild alkaline solution (0.1 M NaOH) was selected as the regenerant. This choice is scientifically grounded: at high pH, the surface of the Zn–Fe LDH/CA composite becomes more negatively charged, creating electrostatic repulsion with the anionic form of CFX (which is deprotonated at its carboxylic group). Furthermore, OH^- ions act as competing anions, displacing the adsorbed CFX molecules from the active sites.[22,57]

This simple method proved highly effective. The desorption efficiency after the first cycle was 96.5%, confirming the efficacy of NaOH in reversing the adsorption process. More importantly, the adsorbent exhibited excellent reusability. As shown in Fig. 11, the removal efficiency of CFX remained above 91% after the second regeneration cycle and retained a high capacity of 85% even after five consecutive adsorption–desorption cycles. The gradual decrease in efficiency after the fifth cycle can be attributed to a minor loss of adsorbent mass during recovery and potential pore blockage by strongly bound CFX molecules or impurities.

The high regeneration efficiency and reusability performance underscore the robustness of the Zn–Fe LDH/CA composite. More importantly, it demonstrates that a straightforward, low-cost chemical regeneration process is sufficient to maintain high performance, significantly enhancing the practical applicability and economic attractiveness of this green adsorbent for long-term water treatment operations.[21,56]

3.8 Greenness of the proposed method

To determine how our analytical methodology can impact the environment and ecosystems, the greenness assessment tools AGREEprep, BAGI, and RGB12 were tested to evaluate how our analytical approach may impact the environment and ecosystems.

AGREEprep[58] thoroughly evaluates how environmentally friendly sample preparation techniques are. Environmentally

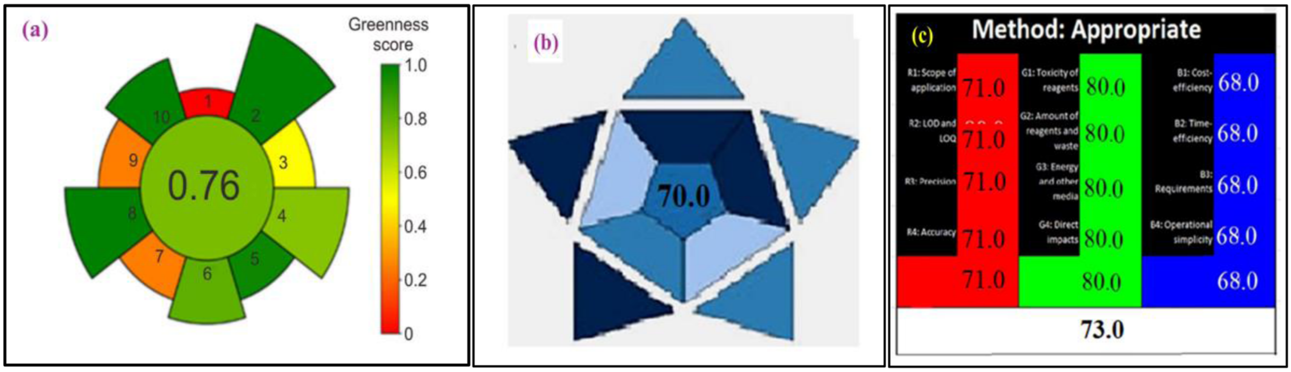

Fig. 12 AGREEprep greenness tool (a); BAGI blueness tool (b); and RGB 12 whiteness tool (c).

friendly configurations for sample post preparation, operator safety, step integration and automation, solvent safety, material sustainability, waste reduction, sample volume reduction, sample throughput maximization, energy consumption reduction, and sample preparation site are all factors that impact sample preparation. Using the 10 GSP principles, a 0–1 scale is developed, and Fig. 12(a) shows the AGREEprep pictogram. The evaluation of each of the ten GSP principles yields the final score (0.76) for the GAC measure.

The BAGI tool[58] is employed to evaluate our method's blueness quantitatively, and the approximate mean of these scores is used to calculate the composite BAGI index. Fig. 12(b) shows the remarkable BAGI ranking of 70.0 that was achieved in this investigation.

Fig. 12(c) demonstrates the RGB-12 algorithm method.[58] The whiteness profile of our proposed method was quantitatively examined. The overall sustainability level of our analytical method produced a good whiteness value of 73.0 and demonstrated the improved performance, dependability, and viability of our suggested strategy from an economic standpoint.

4. Conclusion

This study demonstrates that chia seed-encapsulated Zn–Fe LDH is an effective and stable adsorbent for ciprofloxacin removal, exhibiting high removal efficiency. More importantly, it establishes a novel, holistic approach to water treatment by developing a multifunctional platform that integrates green synthesis, efficient adsorption, real-world application, and waste valorization. Comprehensive characterization confirmed the material's structural integrity before and after adsorption. Adsorption data closely fits Langmuir-based models, indicating monolayer adsorption, with thermodynamic analysis confirming a spontaneous and exothermic process optimized at mild conditions. The work's distinct novelty is underscored by its successful transition beyond the lab: a semi-pilot scale system showed rapid and efficient pharmaceutical contaminant removal in real wastewater, supporting its practical scalability. Furthermore, the material exhibited excellent electrocatalytic activity for methanol oxidation, suggesting a direct path for repurposing spent adsorbent into a cost-effective catalyst and addressing its end-of-life cycle. Cost and green chemistry assessments further emphasize its economic and environmental benefits. Overall, the Zn–Fe LDH/CA composite offers a promising, sustainable, and integrated approach for pharmaceutical wastewater remediation and energy-related applications, differentiating it from studies focused solely on adsorption capacity. The use of chia seed mucilage proved to be a key differentiator, outperforming other natural polymers due to its unique polysaccharide structure, superior adsorption capacity, scalability, multifunctionality, and environmental benignity, as validated by both experimental results and green metrics. Its economic viability ($2.033/g) and non-toxic, biodegradable nature position it as a superior alternative to more costly or less sustainable biopolymers like chitosan.

Ethics approval

Not applicable as the study is not applied on human or animals' study. The article does not include any studies on human participants or animals conducted by any of the authors.

Consent for publication

The authors confirm:

- That the work described has not been published before.
- That it is not under consideration for publication elsewhere.
- That its publication has been approved by all co-authors.

Conflicts of interest

The authors declare no competing interests.

Data availability

The datasets used and/or analyzed during the current study are available from the corresponding author on reasonable request.

Supplementary information is available. See DOI: **https://doi.org/10.1039/d5ra06018d**.

Acknowledgements

This work was supported and funded by the Deanship of Scientific Research at Imam Mohammad Ibn Saud Islamic University (IMSIU) (grant number IMSIU-DDRSP2502).

References

1 S. Ghosh, S. Pourebrahimi, A. Malloum, O. J. Ajala, S. S. AlKafaas, H. Onyeaka, N. D. Nnaji, A. Oroke, C. Bornman, O. Christian, S. Ahmadi and M. Y. Wani, A review on ciprofloxacin removal from wastewater as a pharmaceutical contaminant: Covering adsorption to advanced oxidation processes to computational studies, *Mater. Today Commun.*, 2023, **37**, 107500, DOI: **10.1016/j.mtcomm.2023.107500**.

2 P. Khan, R. Saha and G. Halder, Towards sorptive eradication of pharmaceutical micro-pollutant ciprofloxacin from aquatic environment: A comprehensive review, *Sci. Total Environ.*, 2024, **919**, 170723, DOI: **10.1016/j.scitotenv.2024.170723**.

3 S. Shehu Imam, R. Adnan and N. H. Mohd Kaus, Photocatalytic degradation of ciprofloxacin in aqueous media: a short review, *Toxicol. Environ. Chem.*, 2018, **100**, 518–539, DOI: **10.1080/02772248.2018.1545128**.

4 X. Wang, H. Su and X. Liu, The Impact of Green Technological Innovation on Industrial Structural Optimization Under Dual-Carbon Targets: The Role of the Moderating Effect of Carbon Emission Efficiency, *Sustainability*, 2025, **17**(14), 6313, DOI: **10.3390/su17146313**.

5 A. Avcı, İ. İnci and N. Baylan, A Comparative Adsorption Study with Various Adsorbents for the Removal of

Ciprofloxacin Hydrochloride from Water, *Water. Air. Soil Pollut.*, 2019, **230**, 250, DOI: 10.1007/s11270-019-4315-6.

6 Q. Fang, Q. Sun, J. Ge, H. Wang and J. Qi, Multidimensional Engineering of Nanoconfined Catalysis: Frontiers in Carbon-Based Energy Conversion and Utilization, *Catalysts*, 2025, **15**(5), 477, DOI: 10.3390/catal15050477.

7 C. Jiang, X. Zhang, X. Xu and L. Wang, Magnetic mesoporous carbon material with strong ciprofloxacin adsorption removal property fabricated through the calcination of mixed valence Fe based metal-organic framework, *J. Porous Mater.*, 2016, **23**, 1297–1304, DOI: 10.1007/s10934-016-0188-x.

8 N. Genç, E. C. Dogan and M. Yurtsever, Bentonite for ciprofloxacin removal from aqueous solution, *Water Sci. Technol.*, 2013, **68**, 848–855, DOI: 10.2166/wst.2013.313.

9 N. Dhiman and N. Sharma, Batch adsorption studies on the removal of ciprofloxacin hydrochloride from aqueous solution using ZnO nanoparticles and groundnut (Arachis hypogaea) shell powder: a comparison, *Indian Chem. Eng.*, 2019, **61**, 67–76, DOI: 10.1080/00194506.2018.1424044.

10 M. T. Rahman, F. B. Sagar, M. L. Rahman, F. Rahman, M. M. Rahman Nahid and N. Sharmin, Efficient adsorptive removal of ciprofloxacin from wastewater using alginate bearing Mg–Al layered double hydroxide, *J. Indian Chem. Soc.*, 2025, **102**, 101519, DOI: 10.1016/j.jics.2024.101519.

11 S. Aydin, M. E. Aydin, F. Beduk and A. Ulvi, Removal of antibiotics from aqueous solution by using magnetic Fe 3 O 4/red mud-nanoparticles, *Sci. Total Environ.*, 2019, **670**, 539–546, DOI: 10.1016/j.scitotenv.2019.03.205.

12 B. P. Priyanka, S. Singh and M. Bansal, Superior adsorptive removal of ciprofloxacin by graphene oxide modified Ni-Al layered double hydroxide composites, *J. Alloys Compd.*, 2024, **976**, 173220, DOI: 10.1016/j.jallcom.2023.173220.

13 S. Sohrabnezhad, Z. Poursafar and A. Asadollahi, Synthesis of novel core@shell of MgAl layered double hydroxide @ porous magnetic shell (MgAl-LDH@PMN) as carrier for ciprofloxacin drug, *Appl. Clay Sci.*, 2020, **190**, 105586, DOI: 10.1016/j.clay.2020.105586.

14 R. K. Mahmoud, M. Taha, A. Zaher and R. M. Amin, Understanding the physicochemical properties of Zn–Fe LDH nanostructure as sorbent material for removing of anionic and cationic dyes mixture, *Sci. Rep.*, 2021, **11**, 21365, DOI: 10.1038/s41598-021-00437-w.

15 K. Yang, C. Li, Q. Zhu, H. Wang and J. Qi, Rich Oxygen Vacancies in Bimetallic MnCo2O4.5 Spheres for Enhancing Lean Methane Catalytic Oxidation, *Nanomaterials*, 2025, **15**(7), 524, DOI: 10.3390/nano15070524.

16 M. Li, A. Ali, Y. Li, J. Su and S. Zhang, The performance and mechanism of simultaneous removal of calcium and heavy metals by Ochrobactrum sp. GMC12 with the chia seed (Salvia hispanica) gum as a synergist, *Chemosphere*, 2022, **297**, 134061, DOI: 10.1016/j.chemosphere.2022.134061.

17 F. Neese, F. Wennmohs, U. Becker and C. Riplinger, The ORCA quantum chemistry program package, *J. Chem. Phys.*, 2020, **152**, 224108, DOI: 10.1063/5.0004608.

18 F. Neese, A perspective on the future of quantum chemical software: the example of the ORCA program package, *Faraday Discuss.*, 2024, 295–314, DOI: 10.1039/d4fd00056k.

19 H. T. Ahmed and O. G. Abdullah, Preparation and composition optimization of PEO: MC polymer blend films to enhance electrical conductivity, *Polymers*, 2019, **11**(5), 853, DOI: 10.3390/polym11050853.

20 M. Wojdyr, Fityk: A general-purpose peak fitting program, *J. Appl. Crystallogr.*, 2010, **43**, 1126–1128, DOI: 10.1107/S0021889810030499.

21 N. Bagotia, Regeneration strategies for exhausted adsorbents used in water treatment - A critical review, *J. Water Process Eng.*, 2025, **69**, 106560, DOI: 10.1016/j.jwpe.2024.106560.

22 T. S. Renu, A review on regeneration of adsorbent and recovery of metals: Adsorbent disposal and regeneration mechanism, *S. Afr. J. Chem. Eng.*, 2024, **50**, 39–50, DOI: 10.1016/j.sajce.2024.07.006.

23 A. Zaher, M. Taha and A. Farghali, Zn/Fe LDH as a clay-like adsorbent for the removal of oxytetracycline from water: combining experimental results and molecular simulations to understand the removal mechanism, *Environ. Sci. Pollut. Res.*, 2020, **27**(11), 12256–12269, DOI: 10.1007/s11356-020-07750-3.

24 S. A. A. Moaty, A. A. Farghali and R. Khaled, Preparation, characterization and antimicrobial applications of Zn-Fe LDH against MRSA, *Mater. Sci. Eng. C*, 2016, **68**, 184–193.

25 S. Torbati, P. Yekan Motlagh and A. Khataee, Toxicity of ZnFe-SO4 layered double hydroxide in Tetradesmus obliquus and evaluation of some physiological responses of the microalgae for stress management, *Sci. Rep.*, 2024, **14**, 1–10, DOI: 10.1038/s41598-023-51042-y.

26 Q. Yang, S. Wang, F. Chen, K. Luo, J. Sun, C. Gong, F. Yao, X. Wang, J. Wu, X. Li, D. Wang and G. Zeng, Enhanced visible-light-driven photocatalytic removal of refractory pollutants by Zn/Fe mixed metal oxide derived from layered double hydroxide, *Catal. Commun.*, 2017, **99**, 15–19, DOI: 10.1016/j.catcom.2017.05.010.

27 H. A. Hassanin and A. Taha, Sonochemical-assisted biogenic synthesis of theophrasite β-Ni (OH) 2 nanocluster using chia seeds extract: Characterization and anticancer activity, *Nanomaterials*, 2022, **12**, 1919.

28 H. Mohamed, R. Mahmoud, A. Abdelwahab, A. A. Farghali, F. I. A. El-Ela and A. E. Allah, Multifunctional ternary ZnMgFe LDH as an efficient adsorbent for ceftriaxone sodium and antimicrobial agent: sustainability of adsorption waste as a catalyst for methanol electro-oxidation, *RSC Adv.*, 2023, **13**, 26069–26088.

29 R. Mahmoud, N. M. Kotb, Y. GadelHak, F. I. A. El-Ela, A. Z. Shehata, S. I. Othman, A. A. Allam, H. A. Rudayni and A. Zaher, Investigation of ternary Zn–Co–Fe layered double hydroxide as a multifunctional 2D layered adsorbent for moxifloxacin and antifungal disinfection, *Sci. Rep.*, 2024, **14**, 806, DOI: 10.1038/s41598-023-48382-0.

30 M. Vedanarayanan, C. M. Chen and M. G. Sethuraman, Efficient Hydrogen and Oxygen Evolution: Dual-Functional Electrocatalyst of Zinc Iron Layered Double Hydroxides

and Nickel Cobalt Sulfides on Nickel Foam for Seawater Splitting, *ACS Appl. Energy Mater.*, 2024, **7**, 7260–7271, DOI: **10.1021/acsaem.4c01290**.

31 H. Awes, Z. Zaki, S. Abbas, H. Dessoukii, A. Zaher, S. A. Abd-El Moaty, N. Shehata, A. Farghali and R. K. Mahmoud, Removal of Cu2+ metal ions from water using Mg-Fe layered double hydroxide and Mg-Fe LDH/5-(3-nitrophenyllazo)-6-aminouracil nanocomposite for enhancing adsorption properties, *Environ. Sci. Pollut. Res.*, 2021, **28**, 47651–47667, DOI: **10.1007/s11356-021-13685-0**.

32 M. Manyangadze, N. H. M. Chikuruwo, T. B. Narsaiah, C. S. Chakra, M. Radhakumari and G. Danha, Enhancing adsorption capacity of nano-adsorbents via surface modification: A review, *S. Afr. J. Chem. Eng.*, 2020, **31**, 25–32, DOI: **10.1016/j.sajce.2019.11.003**.

33 S. M. Mahgoub, A. S. Alawam, H. A. Rudayni, A. A. Allam, S. A. A. Abdel Aziz, A. A. Eweis, E. Khaled, R. Shafei, F. Mohamed and R. Mahmoud, Lysozyme-dequalinium encapsulation in a Zn-Fe LDH-chia seed matrix for enhanced antimicrobial dental therapeutics, *RSC Adv.*, 2025, **15**, 30872–30899, DOI: **10.1039/d5ra04212g**.

34 D. Dordevic, J. Hrachovska, S. Dordevic and I. Kushkevych, Impact of saline sprouting on antioxidant properties and bioactive compounds in chia seeds, *Open Life Sci.*, 2025, **20**(1), 20251125, DOI: **10.1515/biol-2025-1125**.

35 E. A. Mohamed, H. M. Ahmed, A. A. Altalhi, H. A. S. Al-Shamiri and N. A. Negm, Highly efficient and rapid removal of Congo red dye from textile wastewater using facile synthesized Mg/Ni/Al layered double hydroxide, *Sci. Rep.*, 2025, **15**, 2183, DOI: **10.1038/s41598-024-84604-9**.

36 K. Mogolodi Dimpe and P. N. Nomngongo, Application of activated carbon-decorated polyacrylonitrile nanofibers as an adsorbent in dispersive solid-phase extraction of fluoroquinolones from wastewater, *J. Pharm. Anal.*, 2019, **9**, 117–126, DOI: **10.1016/j.jpha.2019.01.003**.

37 S. M. Mahgoub, M. R. Shehata, F. L. Abo El-Ela, A. Farghali, A. Zaher and R. K. Mahmoud, Sustainable waste management and recycling of Zn–Al layered double hydroxide after adsorption of levofloxacin as a safe anti-inflammatory nanomaterial, *RSC Adv.*, 2020, **10**, 27633–27651, DOI: **10.1039/d0ra04898d**.

38 A. I. Khan and D. O'Hare, Intercalation Chemistry of Layered Double Hydroxides: Recent Developments and Applications, *J. Mater. Chem.*, 2002, **12**, 3191–3198.

39 E. E. Abdel-Hady, R. Mahmoud, S. H. M. Hafez and H. F. M. Mohamed, Hierarchical ternary ZnCoFe layered double hydroxide as efficient adsorbent and catalyst for methanol electrooxidation, *J. Mater. Res. Technol.*, 2022, **17**, 1922–1941, DOI: **10.1016/j.jmrt.2022.01.042**.

40 E. E. Abdel-Hady, H. F. M. Mohamed, S. H. M. Hafez, A. M. M. Fahmy, A. Magdy, A. S. Mohamed, E. O. Ali, H. R. Abdelhamed and O. M. Mahmoud, Textural properties and adsorption behavior of Zn–Mg–Al layered double hydroxide upon crystal violet dye removal as a low cost, effective, and recyclable adsorbent, *Sci. Rep.*, 2023, **13**, 6435.

41 I. Langmuir, THE ADSORPTION OF GASES ON PLANE SURFACES OF GLASS, MICA AND PLATINUM, *J. Am. Chem. Soc.*, 1918, **40**, 1361–1403, DOI: **10.1021/ja02242a004**.

42 J. Appel, Freundlich's adsorption isotherm, *Surf. Sci.*, 1973, **39**, 237–244.

43 O. Redlich and D. L. Peterson, A Useful Adsorption Isotherm, *J. Phys. Chem.*, 1959, **63**, 1024, DOI: **10.1021/j150576a611**.

44 B. Houri, A. Legrouri, A. Barroug, C. Forano and J.-P. Besse, Use of the ion-exchange properties of layered double hydroxides for water purification, *Collect. Czechoslov. Chem. Commun.*, 1998, **63**, 732–740.

45 Z. Adamczyk and P. Warszyński, Role of electrostatic interactions in particle adsorption, *Adv. Colloid Interface Sci.*, 1996, **63**, 41–149.

46 Y. Liu, Y. Deng, J. Zheng, F. Wu, J. Lu, S. Sun, D. Wu and T. Wu, Role and influence of hydrogen bonds in composite phase change materials: A critical review, *Sol. Energy Mater. Sol. Cells*, 2022, **248**, 112031.

47 F. Tomul, Y. Arslan, B. Kabak, D. Trak and H. N. Tran, Adsorption process of naproxen onto peanut shell-derived biosorbent: important role of n–π interaction and van der Waals force, *J. Chem. Technol. Biotechnol.*, 2021, **96**, 869–880.

48 G. Crini, Recent developments in polysaccharide-based materials used as adsorbents in wastewater treatment, *Prog. Polym. Sci.*, 2005, **30**, 38–70.

49 R. Sure and S. Grimme, Corrected small basis set Hartree-Fock method for large systems, *J. Comput. Chem.*, 2013, **34**, 1672–1685, DOI: **10.1002/jcc.23317**.

50 R. Cammi and B. Mennucci, Linear response theory for the polarizable continuum model, *J. Chem. Phys.*, 1999, **110**, 9877–9886, DOI: **10.1063/1.478861**.

51 R. Baronia, J. Goel, J. Kaswan, A. Shukla, S. K. Singhal and S. P. Singh, PtCo/rGO nano-anode catalyst: enhanced power density with reduced methanol crossover in direct methanol fuel cell, *Mater. Renew. Sustain. Energy*, 2018, **7**, 1–13.

52 R. Abdelazeem, W. Kamal, Z. E. Eldin, M. A. Roshdy, A. A. Allam, S. Saeed, D. A. Tawab, S. I. Othman, A. E. Allah, A. M. Radalla and R. Mahmoud, Exploring the potential of waste biomass of olive as an additive for layered double hydroxide/polyurethane as an effective and safe agent for the adsorption of drug residues: a bioremediation approach, *Mater. Adv.*, 2024, 9092–9106, DOI: **10.1039/d4ma00910j**.

53 P. Das, P. Debnath and A. Debnath, Enhanced sono-assisted adsorptive uptake of malachite green dye onto magnesium ferrite nanoparticles: Kinetic, isotherm and cost analysis, *Environ. Nanotechnology, Monit. Manag.*, 2021, **16**, 100506, DOI: **10.1016/j.enmm.2021.100506**.

54 M. KAMEL, G. A. EL-FATAH, A. ZAHER, A. A. FARGHALI, S. I. OTHMAN, A. A. ALLAM, H. A. RUDAYNI, A. M. SALAH, M. E. M. HASSOUNA and R. MAHMOUD, Cost-effective layered double hydroxides/conductive polymer nanocomposites for electrochemical detection of wastewater pollutants, *Chinese J. Anal. Chem.*, 2024, **52**, 100368, DOI: **10.1016/j.cjac.2024.100368**.

55 M. B. Ahmed, J. L. Zhou, H. H. Ngo and W. Guo, Adsorptive removal of antibiotics from water and wastewater: progress and challenges, *Sci. Total Environ.*, 2015, **532**, 112–126.

56 A. V Baskar, N. Bolan, S. A. Hoang, P. Sooriyakumar, M. Kumar, L. Singh, T. Jasemizad, L. P. Padhye, G. Singh and A. Vinu, Recovery, regeneration and sustainable management of spent adsorbents from wastewater treatment streams: A review, *Sci. Total Environ.*, 2022, **822**, 153555.

57 A. M. Abdelkawy, F. M. Elantabli, R. Mahmoud, S. M. Mahgoub, F. I. A. El-Ela, H. A. Mohamed and S. A. A. Moaty, Enhanced Zn-Co-Fe Layered Double Hydroxides for Effective Levofloxacin Removal: Innovation in Reuse of Waste Adsorbent, *J. Pharm. Innov.*, 2025, **20**, 86, DOI: 10.1007/s12247-025-09988-1.

58 Á. I. López-Lorente, F. Pena-Pereira, S. Pedersen-Bjergaard, V. G. Zuin, S. A. Ozkan and E. Psillakis, The ten principles of green sample preparation, *TrAC Trends Anal. Chem.*, 2022, **148**, 116530.